Physics-based evaluation of the maximum magnitude of potential earthquakes induced by the Hutubi (China) underground gas storage

Guoyan Jiang[1,2], Lin Liu[2], Andrew J. Barbour[3], Renqi Lu[4], and Hongfeng Yang[2]

[1]School of Geodesy and Geomatics, Wuhan University, Hubei, China

[2]Earth System Science Programme, Chinese University of Hong Kong, Hong Kong, China

[3]U.S. Geological Survey, Earthquake Science Center, Calif., USA

[4]Institute of Geology, China Earthquake Administration, Beijing, China

Corresponding author: Guoyan Jiang (guoyanjiang@gmail.com)

Key Points

- Sharp increase of induced seismicity was primarily controlled by poroelastic loading on secondary southwest-dipping thrust faults.
- Slip tendency analyses reveal low reactivation potential of the largest Hutubi fault hydraulically connected to injection wells.
- The largest potential event would most likely occur on secondary faults in regions where poroelastic loading promotes frictional failure.

This article has been accepted for publication and undergone full peer review but has not been through the copyediting, typesetting, pagination and proofreading process, which may lead to differences between this version and the Version of Record. Please cite this article as doi: 10.1029/2020JB021379.

Abstract

The world's largest underground gas storage facility in Hutubi (HUGS), China, is a unique case where cyclic gas injection-extraction induced both seismicity and ground deformation. To assess the potential for future induced seismicity, we develop a framework physically based on a well-constrained hydro-geomechanical model and on fully coupled poroelastic simulations. We first interpret the spatiotemporal distribution and focal mechanisms of induced earthquakes and use these to estimate the magnitude and location of the largest potential earthquake. The sharp increase in seismicity was controlled by poroelastic loading on secondary southwest-dipping thrust faults with spatial scales too small to be resolved by 3D seismic surveys. Both operational and local geological factors affect the seismic productivity at the HUGS site, distinguishing it from most cases of seismicity induced by wastewater disposal and hydraulic fracturing. We then conduct slip tendency analyses for major faults imaged by the seismic data, including the largest reservoir-bounding Hutubi fault hydraulically connected to injection wells. The reactivation potentials of these imaged faults are estimated to be extremely low. Accordingly, future seismicity would most likely occur on failure-prone secondary faults in regions with positive stress perturbation due to poroelastic loading. The maximum magnitude likely depends on the spatial scales of the secondary faults. As the occurrence of detected earthquakes is spatially and temporally consistent with the simulated evolution of Coulomb stress perturbation, the location of the largest potential earthquake probably depends on the sizes of the poroelastic stressing regions.

Plain Language Summary

Across the world there are numerous underground gas storage (UGS) facilities that are either under construction or planned due to major demands for clean energy and major concerns over tackling issues related to global climate change. Induced seismicity at UGS facilities is a burgeoning topic, with few documented cases so far. In some cases UGS facilities are located in highly-populated regions that could experience strong ground shaking due to local and shallow induced earthquakes. Under the typical scenario of earthquakes induced by pore pressure diffusion, the maximum magnitude is sometimes thought to be governed by fluid-stimulated rock mass or the volume of injected fluids. However, in the case of earthquakes induced by poroelastic effects (rock deformation beyond the overpressure front), we know very little about the influence of additional critical parameters on the timing, location, and magnitude of induced earthquakes. The largest potential earthquake associated with the HUGS is a problem compounded by the effects from

pressure and poroelastic perturbation. Our study helps to fill in the knowledge gap between pore pressure and poroelastic effects, and provides a reference to assess and mitigate the risk of seismicity related to UGS operations.

1 Introduction

The Hutubi underground gas storage (HUGS) facility is located in a transition zone between the northern Tien Shan and the southern Junggar Basin in northwest China (Figure 1a). The subsurface repository was transformed from a depleted natural gas reservoir, which had been producing gas for about 14 years, from 1998 to 2012. During that time, the pressure within the reservoir decreased from ~34 MPa to ~13.2 MPa (*Cao, 2013*). Field tests of gas concentrations in wells near the repository revealed that it had retained its excellent natural sealing ability after the depletion (*Pang et al., 2012*). The design capacity of the HUGS facility is up to 10.7 billion m^3 (*Cao, 2013*) (Figure 1b), making it the largest storage capacity in the world. The maximum working pressure of the reservoir is set to be 34 MPa, equal to the initial pressure before exploitation of the gas field in 1998. Therefore, the possibility of reservoir overpressurisation threatening the caprock integrity (*Dempsey et al., 2014*) is expected to be quite low.

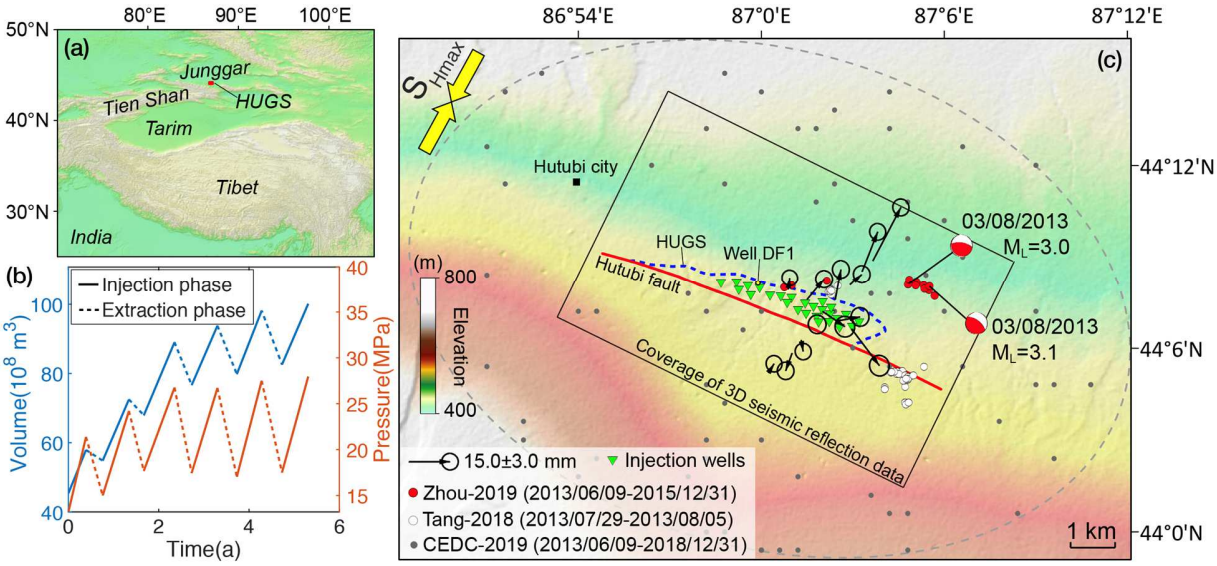

Figure 1. The Hutubi underground gas storage (HUGS) facility. (a) Tectonic setting of the HUGS. (b) Variations of gas volumes and measured pore pressure within the reservoir from the first to sixth injection phase. The initial gas volume and pressure within the reservoir are 4.53 billion m^3 and ~13.2 MPa, respectively. In contrast, the design capacity and maximum working pressure are 10.7 billion m^3 and 34 MPa, respectively. (c) Induced seismicity and ground deformation. Black arrows plot horizontal ground displacements observed by 13 campaign GPS stations from 2014/03/28 to 2017/11/18 (*Jiang et al. 2020*). The gray dashed ellipse is about 15 km off the HUGS and used to select potential induced earthquakes from

China Earthquake Data Center (CEDC). Well DF1 provides sonic logging and drilling data for geological interpretation of 3D seismic reflection data.

Since the operation commenced on 9 June 2013, observations of both seismicity and ground displacements have been demonstrably linked to cyclic gas injection-extraction (*Jiang et al., 2020; Qiao et al., 2018; Tang et al., 2018; Zhou et al., 2019*). Two $M_L \geq 3.0$ earthquakes occurred in August 2013, only two months after the operation (Figure 1c). A local Global Positioning System (GPS) network detected horizontal ground extension on the order of centimeters (~0.9 cm/yr) due to gas injection at depths of ~3.6 km, which coincides with the response of a sealed reservoir with pressure build-up (*Jiang et al., 2020*). Accordingly, the effect of loading from cyclic reservoir dilatation was considered to be a causal factor for the seismic cluster relocated by Zhou et al. (*2019*) at ~2 km northeast of the HUGS in August 2013 (Figure 1c) (*Jiang et al., 2020*).

Despite the abundance of geophysical observations, the physical mechanism behind the spatial and temporal distribution of induced seismicity at the HUGS site, and estimates of the magnitude and location of the largest potential earthquake, are still in doubt. In particular, the largest earthquake magnitude is a crucial parameter of seismic hazard analysis owing to its strong influence on the exceedance probability of ground motion. Determination of the magnitude and location is a fundamental challenge but is helpful to improve the accuracy of hazard assessments for induced earthquakes (e.g., *Ellsworth, 2013; McGarr et al., 2015; Yeck et al., 2015; Petersen et al., 2018*). Current statistical models for the maximum magnitude can predict an increase in the frequency of felt events (e.g., *van der Elst et al., 2016*), but they cannot locate specific faults that might be responsible for future seismicity.

Considering that the current operational cycle of the HUGS is sufficient to induce earthquakes and has not yet reached the maximum working capacity (Figure 1b), it is plausible that any future operation in excess of present capacity could induce larger earthquakes under the physical mechanism of poroelastic loading associated with the reservoir dilation and contraction. Moreover, the 16-km-long Hutubi fault, bisecting the reservoir and acting as a barrier to gas transport (*Pang et al., 2012*), inevitably suffers from pressure perturbations during cyclic gas injection-extraction, thus giving rise to another potential of fault reactivation. A full-length rupture could lead to a destructive earthquake with a magnitude around Mw 6.3 (*Blaser et al., 2010*), which would constitute one of the largest induced earthquakes on record. These two potentials make forecast of

the largest potential earthquake at the HUGS site a problem compounded by the effects of both pressure and poroelastic stress perturbation.

In the case of earthquakes induced by pore pressure perturbation, the maximum magnitude has been regarded to be governed by the volume of fluid-stimulated rock (*Shapiro et al., 2011*) or injected fluids (*McGarr, 2014*). In contrast, *van der Elst et al (2016)* argue that the magnitudes of induced earthquakes can be as large as allowed by the tectonic setting and the Gutenberg-Richter distribution: injection and tectonic factors (stresses and faults) control the earthquake nucleation and magnitude, respectively. Based on recent earthquake dynamic rupture simulations, the state of absolute stress can influence the rupture behavior of induced earthquakes: ones nucleating by localized pore pressure perturbations are likely self-arresting in low shear stress environments (*Cappa & Rutqvist, 2011; Galis et al., 2017; Norbeck & Horne, 2018*), which may explain why the maximum magnitudes in many cases of induced seismicity are linked to injection parameters rather than tectonic factors. However, some recent induced earthquakes in high tectonic stress environments like the 2017 Mw 5.5 Pohang (Korea) earthquake (*Lee et al., 2019*) appear to have ruptured beyond the pressurized fault zones. By comparison, the controlling factors on the maximum magnitude of earthquakes induced by rock deformation beyond the overpressure front (poroelastic effect) remain poorly understood. The HUGS case sheds light on how to estimate the magnitude of the largest potential earthquake induced by poroelastic effects.

Recent efforts on forecasting the magnitude of the largest potential earthquake have been made mainly using statistical and physics-based probabilistic methods, which were applied both theoretically (*Mazzoldi et al., 2012; Dieterich et al., 2015; van der Elst et al., 2016; Maurer & Segall, 2018*) and in practice. Some notable case studies include the Basel (Switzerland) Enhanced Geothermal System (EGS) project (*Afshari Moein et al., 2018*), The Geysers (United States) geothermal field (*Kwiatek et al., 2015*), wastewater disposal in Oklahoma and Kansas (United States) (*Langenbruch & Zoback, 2016; Langenbruch et al., 2018; Norbeck & Rubinstein, 2018; Zhai et al., 2019*), and depletion and compaction of the Groningen (Netherlands) gas field (*Zöller & Holschneider, 2016; Dempsey & Suckale, 2017; Candela et al., 2019; Richter et al., 2020*). The majority of these studies are heavily reliant on earthquake catalogs, with limited consideration of the relationship between the spatial distribution of induced seismicity to realistic pore pressure diffusion and/or poroelastic loading processes. In this study, we take physical interpretation of

both spatial and temporal distribution as well as focal mechanisms of induced earthquakes as a premise to evaluate both the magnitude and location of the largest potential earthquake.

In addition, there are many UGS facilities that are either under construction or planned across the world. This represents a potentially looming crisis since UGS operations can expose local communities to the potential risks of surface deformation and induced seismicity (*Priolo et al., 2015; Gaite et al., 2016; Tang et al., 2018; Zhou et al., 2019; Jiang et al., 2020*). Moreover, induced earthquakes in populated areas caused by other anthropogenic fluid injection and extraction activities appear to be growing in scale and frequency (e.g., *McGarr et al., 2015*; *Chen et al., 2017; Lee et al., 2019; Lei et al., 2019; Wang et al., 2020*). Recent attempts to control the size of induced earthquakes at two EGS sites have been successful (near Helsinki, Finland; *Kwiatek et al., 2019*) but also disastrous (Pohang, Korea; *Kim et al., 2018*). These two cases accentuate the need for timely advancements in methods used to assess and manage evolving risk. Rutqvist et al. *(2016)* emphasize that a best-practice framework is necessary to investigate induced seismicity based on the lessons learned from deep underground carbon dioxide (CO_2) injection. With an abundance of seismic, geodetic, and geologic data available, the HUGS represents an opportunity to conduct detailed analyses of the physical processes leading to induced earthquakes as well as to develop a physics-based strategy to assess seismic risk.

The remainder of this paper is organized as follows. First, a physics-based framework is developed in Section 2 to simultaneously interpret the spatiotemporal distribution and focal mechanisms of induced earthquakes and to assess the largest potential earthquake. Then, we present a variety of data including earthquake catalogs, dense 3D seismic reflection and production data in Section 3. Following the framework, we simulate the spatiotemporal evolution of stress perturbation (pore pressure and Coulomb failure stress) associated with cyclic gas injection-extraction of the HUGS in Section 4 to interpret the observed seismicity, evaluate the reactivation potential of major faults identified by 3D seismic survey, and then make an assessment of the magnitude and location of the largest potential earthquake that might occur in the future. Finally, we conduct sensitivity tests to investigate the influences of model parameter settings on our results.

2 Physics-based framework of assessing the largest potential earthquake

We develop a physics-based framework to first interpret the spatiotemporal distribution and focal mechanisms of induced earthquakes and then estimate the magnitude and location of the largest potential earthquake (Figure 2). A hydro-geomechanical model constrained by multiple geophysical, geologic, and geodetic observations (*Jiang et al., 2020*) is applied to simulate cyclic gas injection-extraction of the HUGS based on fully-coupled poroelasticity (*Rice and Cleary, 1976; Wang, 2000*). Then, spatiotemporal evolution of pore pressure and Coulomb stress perturbation is derived from numerical simulations and used to interpret detected earthquakes. If valid physical interpretation is achieved, we then assess the location and magnitude of the largest potential earthquake, respectively, through two paths. If not, we go back to check the hydro-geomechanical model and earthquake catalogs.

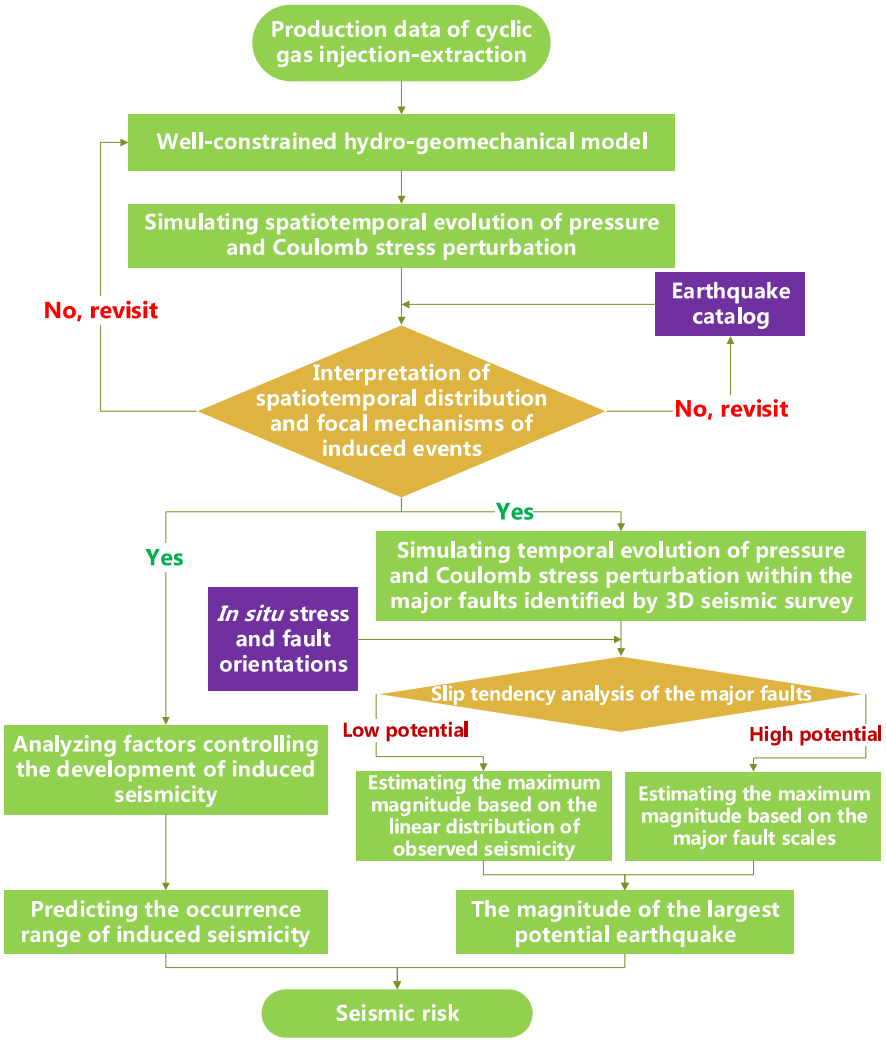

Figure 2. Physics-based framework to estimate the magnitude and location of the largest potential earthquake at the HUGS site. Two yellow diamonds are used to judge whether the physical interpretation is achieved and the reactivation potential of major fault, respectively.

The physical logic of the left path is that if the simulated stress perturbation can interpret the spatial distribution of observed seismicity, we can thus use it to estimate the occurrence range of future induced seismicity. In the right path, we first simulate the temporal stress variations within the major faults identified by 3D seismic survey, and then evaluate the reactivation potentials of the faults based on the method of slip-tendency analysis (*Morris et al., 1996; Streit & Hillis, 2004*). If they are reactivated, the magnitude of the largest earthquake would depend on their spatial scales; otherwise, we estimate the maximum magnitude based on the fault lengths illuminated by seismic clusters. The step of seismicity interpretation consolidates the physical base of final evaluation results. With all major faults identified and mapped, evaluation of the maximum magnitude largely depends on determining the spatial scales of the faults that are most likely to slip; this is independent of the competing models for injection induced earthquakes (e.g., *McGarr, 2014; van Der Elst et al., 2016; Galis et al., 2017*).

2.1 Well-constrained hydro-geomechanical model

Guided by seismic reflection profiles, a local velocity model, rock physics measurements, drilling and logging data, Jiang et al. (*2020*) formulated a 2D hydro-geomechanical model for the HUGS, which extends over a width of 36 km and a depth of 14 km to minimize boundary effects. The model comprises seven layers: Upper Aquifers 1-2, Upper Layer 3, Caprock Layer, Reservoir Layer, and Basal Layers 1-2 (Figure S1). At the HUGS center, the reservoir layer is located between 3.53 km and 3.64 km below the surface. The storage repository is about 2.2 km wide and bounded on the southwest by the Hutubi fault. Based on results from previous field tests (*Pang et al., 2012*) and operational stability of the gas field (*Cao, 2013*), the fault is treated as an impermeable seal with a thickness of 10 m. The surrounding rock layers are assumed to be isotropic porous media. The reservoir porosity and permeability have been calibrated through a grid search procedure based on observations of horizontal ground extension and well pressure changes (*Jiang et al., 2020*); they fall in narrow ranges of 20-30% and 1.25-3.25 × 10^{-13} m^2, respectively. Here we select a pair (porosity = 20%, permeability = 3.25 × 10^{-13} m^2) within the domain to conduct subsequent numerical simulation. Table S1 lists the elastic moduli, porosity and

permeability of each layer and faults as well as fluid properties. Additional technical details on the model building process can be found in Jiang et al. (*2020*).

Although the hydro-geomechanical model is not 3D, the 2D approximation is adequate for the analysis of deformation and stress associated with induced earthquakes that involve reverse or normal faulting (e.g., *Mazzoldi et al., 2012; Segall & Lu, 2015; Chang & Segall, 2016; Zbinden et al., 2020*). For strike-slip faulting a 3D model may be necessary, but Zhou et al. (*2019*) have concluded that the induced earthquakes at the HUGS site developed by reverse faulting. In addition, Figure 1c shows the extension of injection wells parallel to the Hutubi fault, which indicates that a 2D model perpendicular to the fault is a reasonable approximation. On the other hand, although we have attempted to integrate all relevant data to develop the hydro-geomechanical model, it is not clear that the database is sufficiently comprehensive to develop a robust 3D model. Moreover, incomplete production data (Section 3.3) also makes realistic 3D geomechanical modeling impossible.

2.2 Fully-coupled poroelasticity

The theory of poroelasticity couples fluid diffusion with elastic deformation. The basic theory for porous media was initially introduced by the pioneering work of Biot (*1941*), and later reformulated in a more physically rigorous manner by Rice & Cleary (*1976*). The governing equations of fully-coupled isothermal poroelasticity consist of two parts: (I) the Navier-Stokes equation describing quasi-static equilibrium of the solid matrix of porous medium (with shear modulus G, Poisson's ratio ν, permeability k and porosity ϕ),

$$G\nabla^2 u_i + \frac{G}{1-2\nu}\frac{\partial^2 u_k}{\partial x_i \partial x_k} = \alpha\frac{\partial p}{\partial x_i} - F_i, \quad (1)$$

and (II) the mass conservation equation describing the Darcian flow of fluid (with density ρ_f, viscosity η and bulk modulus K_f) within porous rock,

$$S_\varepsilon \frac{\partial p}{\partial t} - \frac{k}{\eta}\nabla^2 p = \frac{Q_m}{\rho_f}, \quad (2)$$

where u_i is displacement component in direction x_i of a Cartesian coordinate system. The quantities p and F_i are pore pressure and body force, respectively. The Biot-Willis coefficient, α, corresponds to the effective stress coefficient for bulk deformation, controlling the magnitude of

poroelastic strain induced by fluid injection. Q_m is the mass source/sink term. The expression of the constrained specific storage coefficient S_ε can be formulated as (*Segall, 2010*),

$$S_\varepsilon = \frac{\alpha}{K_s} + \phi\left(\frac{1}{K_f} - \frac{1}{K_\phi}\right), \quad (3)$$

where $\frac{1}{K_s}$ and $\frac{1}{K_\phi}$ are unjacketed bulk and pore compressibilities, respectively. Equation (3) shows that the storage coefficient depends on not only the elastic moduli of the porous medium but also the fluid properties.

We employ the COMSOL Multiphysics® software package (version 5.6, https://www.comsol.com/) to solve the governing equations. The porous media is assumed to be isotropic and microscopically homogeneous, which indicates $\frac{1}{K_s}$ equal to $\frac{1}{K_\phi}$. In addition, we set the HUGS reservoir to be saturated with natural gas based on the fact that there were still 4.53 billion m^3 gas left in the reservoir after the cease of production of the gas field in 2012. Natural gas is trapped by buoyancy, and overlies the water in the system. The viscosity η and bulk modulus K_f of the gas are set at pressure and temperature conditions (T=50°C, P=20 MPa) (Table S1) to be consistent with practical operations. Outside of the reservoir, the rock is saturated with water, also with constant fluid properties under the specific pressure and temperature. This setting is supported by reports that the volumes of water coming out during the extraction phases are very small: the effect of multi-phase flow is expected to be minor.

2.3 Formulations of thermoelasticity

In addition to the poroelastic effect arising from the coupling between fluid pressure diffusion and elastic deformation, temperature contrasts between injected gas and the reservoir can also influence simulation results. The thermal effect is comprised of two aspects: (I) changes to the fluid properties of gas including viscosity η and bulk modulus K_f, and (II) thermoelastic coupling that causes deformation of solid matrix, especially in locations where the temperature difference is largest, like in the reservoir.

The first influence – changes in fluid properties – is expected to have lesser impact for three reasons. First, natural gas is injected during warm seasons. The temperatures of injection and extraction gas vary from 12°C to 58°C and from 18°C to 61°C (Figure 3), respectively, which can

cause ~20% changes of gas density and viscosity under the pressure of 20 MPa. But the median values of injection and extraction temperatures only differ by 1°C. Second, given that the fluid properties enter only in the context of the hydraulic diffusivity, the impact of their pressure and temperature dependences will likely be much less in comparison with the dominant effect of permeability, which changes by orders of magnitude from layer to layer in the model. Third, in our model the fluid properties of natural gas have been determined based on specific temperature and pressure (Table S1) consistent with practical operations.

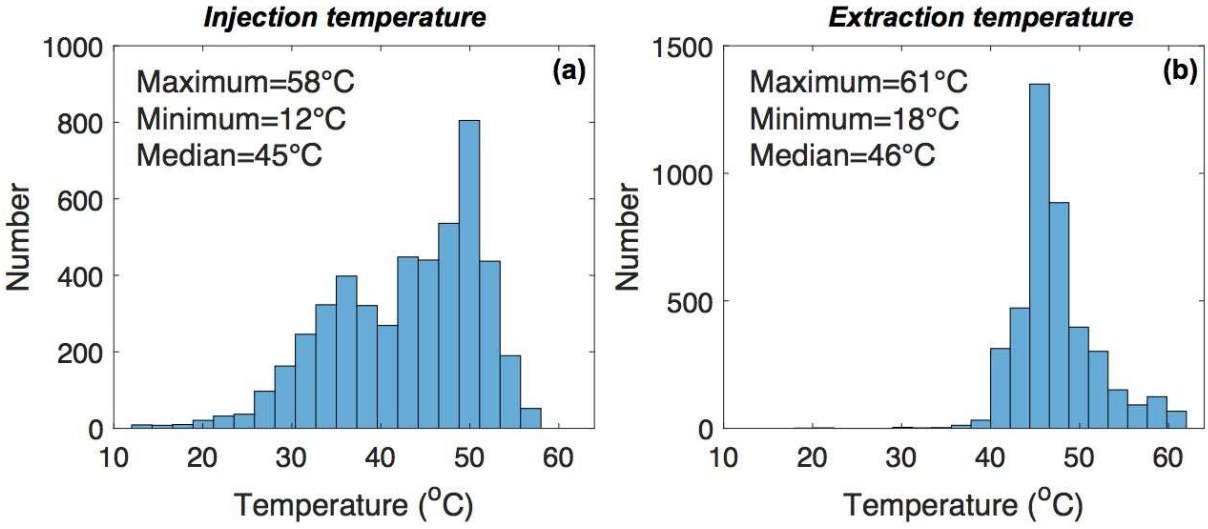

Figure 3. Statistical histograms of temperatures of injection and extraction gas from production data available from 1 June 2016 to 30 April 2017.

The second influence is generally known as the thermoelastic effect, consisting of two parts. First, heat transfer in porous media through conduction of fluid-solid mixture and convection of fluid flow obeys the energy conservation equation. Assuming local thermal equilibrium between fluid (with specific heat C_f and thermal conductivity κ_f) and rock (with density ρ_s, specific heat C_s and thermal conductivity κ_s), and neglecting the dissipation of mechanical energy due to deformation of the solid, the equation is given by

$$\left(\phi\rho_f C_f + (1-\phi)\rho_s C_s\right)\frac{\partial T}{\partial t} + \rho_f C_f \nabla\cdot \boldsymbol{q}T - (\phi\kappa_f + (1-\phi)\kappa_s)\nabla^2 T = Q_e, \qquad (4)$$

where T is the temperature of the fluid-solid mixture, and Q_e is an external energy source. $\boldsymbol{q}$ is the Darcy flux, which can be expressed as $k\rho_f/\eta\,\nabla p$ without consideration of the gravitational

potential and has been involved in equation (2). The second part is also a mechanical equilibrium equation. Taking into account the thermoelastic effect, equation (1) should be rewritten into

$$G\nabla^2 u_i + \frac{G}{1-2\nu}\frac{\partial^2 u_k}{\partial x_i \partial x_k} = \alpha\frac{\partial p}{\partial x_i} + \beta K\frac{\partial T}{\partial x_i} - F_i, \quad (5)$$

where β is the volumetric expansion coefficient of the rock, and K is the drained bulk modulus of the porous media.

We also employ COMSOL Multiphysics® to solve the thermoporoelasticity problem. Both direct observational constraints on the thermophysical properties of rocks of subsurface formation, and the precise history of gas temperatures are unavailable. Hence to assess thermal effects of cyclic gas injection and extraction on the spatiotemporal evolution of pore pressures and Coulomb stress perturbations, we first conduct simulations based on fully-coupled poroelasticity, and then compare them with thermoporoelastic simulations in Section 5.2 based on several groups of thermophysical parameters.

2.4 Calculation of Coulomb failure stress perturbation

The formula to calculate Coulomb stress changes (e.g., King et al., *1994*) is

$$\Delta CFS = \Delta\tau + \mu(-\Delta\sigma_n + \Delta p), \quad (6)$$

where $\Delta\tau$ and $\Delta\sigma_n$ are shear and normal stress changes, respectively, Δp is the change in pore pressure, and μ is the static friction coefficient. Compressive stresses are defined to be positive. Equation (6) can also be rearranged as,

$$\Delta CFS = \Delta PS + \mu\Delta p\ , \quad (7)$$

to isolate the poroelastic stress, ΔPS, equal to $\Delta\tau - \mu\Delta\sigma_n$, from the direct influence of pore pressure changes. In subsequent numerical simulations, we set the orientations of receiver faults based on observational constraints from focal mechanisms of induced earthquakes, geometries of the Hutubi fault and regional background stress regime.

2.5 Calculation of fault slip tendency

The expression of fault slip tendency (Morris et al., *1996*; Streit & Hillis, *2004*) is

$$S_T = \tau/(C + \sigma_n - p), \quad (8)$$

where C denotes the cohesive strength of faults, and the remaining symbols on the right side are the same as those in equation (6). It is worth noting that the stresses in equation (8) are absolute rather than relative. Hence, the slip tendency value depends on local stress regime, fault orientations, simulated pore pressure and elastic stress changes. Slip tendency analysis can help identify the faults with high reactivation potential in a region of perturbed stress, although some caution is warranted as recent studies suggest that induced earthquakes may occur on faults with low reactivation potential (e.g., Cochran, et al., 2020).

At the HUGS site, the magnitudes of the *in situ* stresses have been estimated from borehole breakouts and drilling-induced tensile fractures on image logs by *Cao (2013*); however, they present these in units of specific gravity (*sg*). We only know the ratio of the maximum horizontal principal stress (S_{Hmax}) to the vertical stress (S_V) ranging from 1.06 to 1.23. To re-estimate their absolute values, we first calculate the vertical stress through integrating the densities from the refined local velocity model (used to determine the mechanical parameters of subsurface formation in *Jiang et al., 2020*) over depths based on the method proposed by McGarr & Gay (*1978*). The calculation reveals that the magnitude of S_V at the reservoir depth of 3.6 km is 79.3 MPa. The magnitude of S_{Hmax} is thus equal to 98.3 MPa with an extreme ratio of 1.24, which is favorable to thrust faulting under the current stress regime. Furthermore, the shear and normal stress acting on the fault plane can be calculated according to the following two equations

$$\tau = \frac{\sigma_1 - \sigma_3}{2} \sin 2\delta, \tag{9a}$$

$$\sigma_n = \frac{\sigma_1 + \sigma_3}{2} - \frac{\sigma_1 - \sigma_3}{2} \cos 2\delta, \tag{9b}$$

where σ_1 and σ_3 are the maximum and minimum principal stresses, corresponding to S_{Hmax} and S_V, respectively, and δ is the fault dip angle.

3 Data

3.1 Earthquake catalogs

To examine the temporal and spatial variations of induced seismicity, we gather three catalogs, from Tang et al. (*2018*), Zhou et al. (*2019*) and China Earthquake Data Center (CEDC). Both Tang et al. (*2018*) and Zhou et al. (*2019*) relocated earthquakes with magnitudes of $M_L \geq 1.0$ in the first two injection-extraction cycles as well as the third injection phase (Figure S2). Whereas Tang et

al. (*2018*) only analyzed regional seismological data from permanent stations in the Xinjiang province, Zhou et al. (*2019*) included more data from a temporary network comprising 38 mobile stations. Consequently, Zhou et al. (*2019*) were able to better resolve the location and spatial clustering of the events associated with the first and second injection phases and to determine the focal mechanism solutions of the two largest events in August 2013 (Figure 1c). The catalog retrieved from CEDC comprises $M_L \geq 0.1$ earthquakes up to 31 December 2018 with a horizontal location precision of ~15 km (Figures 1c and 4). Here, we refer to these three independently-derived earthquake catalogs as Tang-2018, Zhou-2019, and CEDC-2019, respectively.

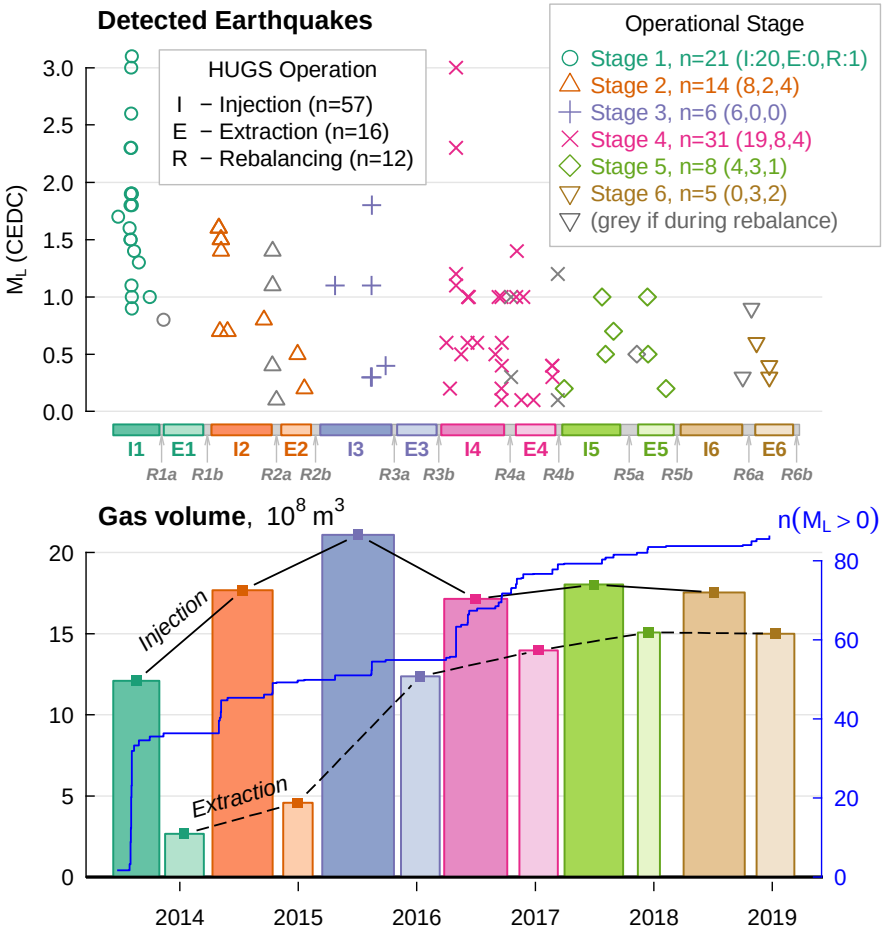

Figure 4. Temporal variations of induced seismicity detected by CEDC and gas volumes. Top: Earthquake numbers (enclosed by parenthesis) in each operational stage including an injection phase (I), an extraction phase (E), and two rebalancing phases (R-a & b). Bottom: Gas volume change of each injection/extraction phase with the cumulative number of earthquake detections overplotted.

All three catalogs show more frequent occurrences of earthquakes in the injection phases as opposed to the extraction or rebalancing phases (Figure 4). To test this, we perform Chi-squared analysis of contingency tables computed for the CEDC-2019 catalog. In particular, we test a two-way table for earthquakes grouped by the type of operation occurring at their origin time (e.g., injection) and the stage number (e.g., injection stage 1). The test results indicate a *p*-value of 0.0041, which is further verified by Monte Carlo simulation (*Hope, 1968*) with 3000 replications; this is strong evidence that the possibility of injection being the primary driver of induced seismicity cannot be rejected.

Despite this evidence, that the injection process was causing most of the earthquakes surrounding the HUGS, we see no correlation with either injection rates or injected volumes. This finding stands in contrast to seismicity induced by wastewater disposal or hydraulic fracturing, which show relatively tight association with injection rates (*Keranen et al., 2014; Weingarten et al., 2015*) or volumes (*Schultz et al., 2018*), respectively.

We further analyze the spatial distribution of induced seismicity based on the catalog of Zhou-2019, whose locations are belived to be more accurate than Tang-2018 and CEDC-2019. Zhou et al. (*2019*) detected the seismic cluster in August 2013 and 3 events in the second injection phase, which are far fewer than the events from Tang et al. (*2018*). To make a clear comparison, Figure 1c only plots the events of the cluster in the Tang-2018 catalog. Both Zhou-2019 and Tang-2018 show that the spatial distribution is characterized by dense clustering and also some sporadic earthquakes. The earthquakes that were tightly clustered in space and time simultaneously lead to sharp increases of seismicity and contribute most to the total number of events (Figure 4). The cluster of events that unambiguously occurred during the first injection phase illuminates a previously-unmapped fault that lies parallel to the Hutubi fault, with a length around 1 km. Although Zhou et al. (*2019*) did not report earthquake location uncertainties, both Tang et al. (*2018*) and Zhou et al. (*2019*) relocated this cluster to ~2 km off the HUGS (Figure 1c).

3.2 3D seismic reflection data

To identify faults in the study area, we analyze 3D seismic reflection data from PetroChina (Figure 5a), which is approximately 15 km long (East-West), 18 km wide (South-North), and more than 9 km deep. Ten seismic reflection profiles spaced equally along the strike of the Hutubi fault (Figure

S3) are extracted from the 3D seismic data to identify major structures and sedimentary layers of the Hutubi anticline. For each profile, we use software Skua-Gocad® to label subsurface layers with artificial synthetic records, well drilling and logging data. First, sonic logging data of drilling well DF1 (Figure 5b) is analyzed to derive Ricker wavelets, which are used to simulate seismic waves. Second, we match the artificial seismic waves surrounding well DF1 with the simulated waves. Lastly, based on the drilling data of well DF1, we can ascertain the subsurface layers.

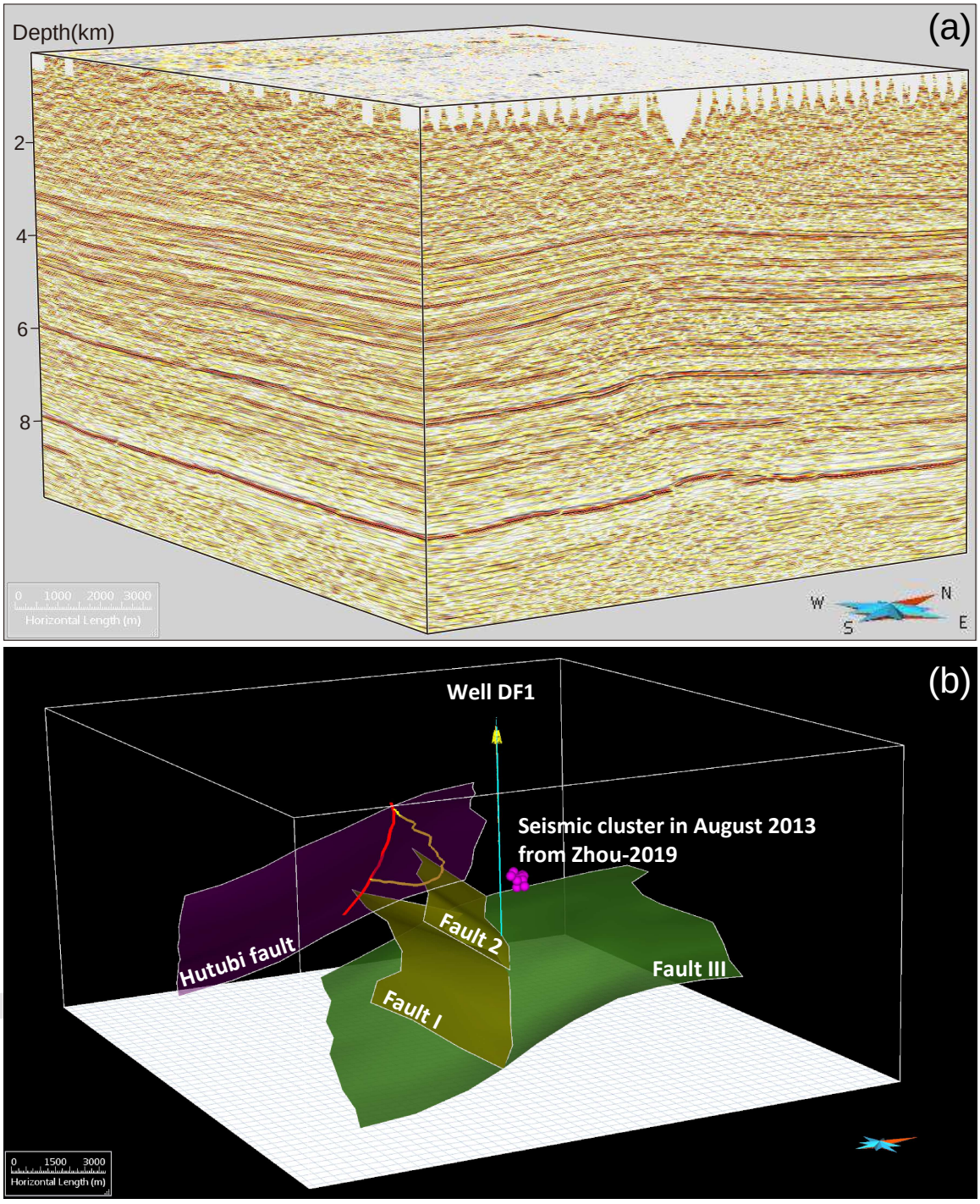

Figure 5. 3D seismic reflection data at the HUGS site (a) and geological interpretations (b). Yellow curve in panel b outlines the spatial range of the HUGS reservoir. Red line marks the intersection between the Hutubi fault and the reservoir.

We further apply the theory of fault-related folds (*Suppe, 1983*; *Shaw et al., 2005*) to interpret the synthetic seismograms of the ten profiles. The depths of seismic profiles are first converted from travel time to the unit of kilometer using an average velocity model (3.0 km/s). Then, major faults and sedimentary layers derived from each profile are used to build a surface model of faults and layers (Figure 5b) with the discrete smooth interpolation algorithm (*Wu et al., 2016, Lu et al., 2019*). We find that the 3D seismic survey data can illuminate several faults with lengths larger than 10 km in the study region. However, it is hard to ascertain smaller faults (*Schultz et al., 2020; Atkinson et al., 2020*), which are always characterized with tiny offsets. Although we can use some methods to derive such small-scale faults (e.g., *Maerten et al., 2006*), the resulting number of small faults would be very large and have a large uncertainty.

The seismic interpretation results show two kinds of shallow-dipping thrust faults within the study area. Above the HUGS reservoir, the Hutubi fault and fault III are associated with the anticlinal topography and dip to the southwest with angles varying from 10° to 25°. Below the reservoir, there are another two faults dipping to the northeast with angles from 22° to 39°, but no distinct faulting features are found near the location of the seismic cluster in August 2013 (*Zhou et al., 2019*). The causative faults are probably secondary faults with scales less than current seismic imaging limits or with slip rates immeasurable by present set of data. From here on we refer to the identified faults as “major faults” and unresolved potential faults as “secondary faults”, respectively.

3.3 Production data

We use the mean gas injection/extraction rate of each phase to simulate the cyclic operation of the HUGS. The mean rates of the first four injection-extraction cycles have been presented by Jiang et al. (*2020*) based on production data of 11 wells from 2015/01/01 to 2017/04/30 as well as online reports on the total gas volume and time span of each phase. Here, we search more online reports to constrain the mean rates for the 5^{th} and 6^{th} injection-extraction cycles (Table S2). In addition, we consider two kinds of production data to forecast the spatiotemporal evolution of stress perturbation for numerical simulations of 20 years in Section 4. (I) The mean rates of the 7^{th} to 20^{th} cycles are set to be same as those of the 6^{th} cycle (Figure 6a). (II) To make the downhole pressure of injection wells reach the maximum working pressure of 34 MPa (*Cao, 2013*) at the end of the

7^{th} injection phase, its injection rate is set to be 6×10^5 kg/d. Rate of the 7^{th} extraction phase is set to be close to the values of the 5^{th} and 6^{th} extraction phases (Figure 6b). For the other cycles (8^{th} to 20^{th}), their rates are set to maintain stable operations of the HUGS. The time spans of injection and extraction phases in forecast simulations are assumed to be equal to the average operation days of the 4^{th} to 6^{th} cycles. Operationally, there is a rebalancing phase (mainly for equipment maintenance) between each injection and extraction phases lasting about three weeks.

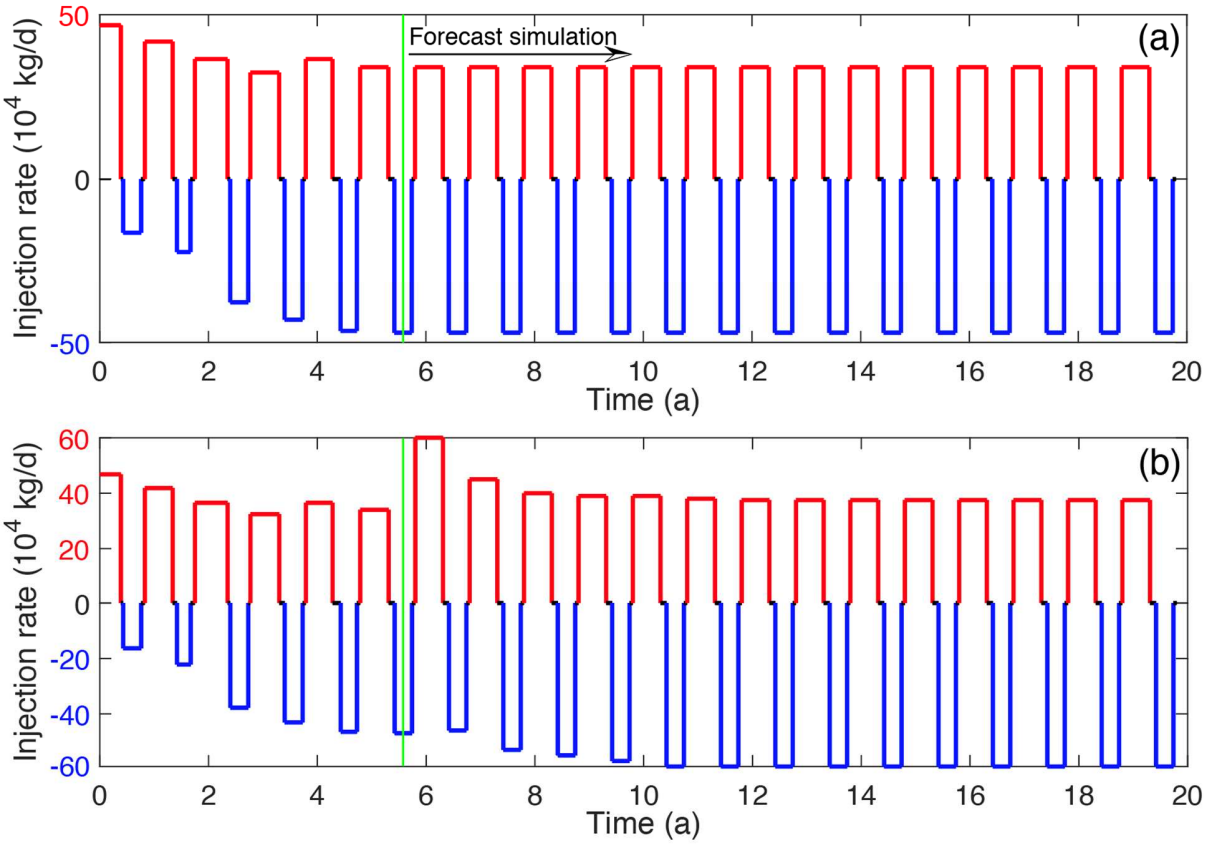

Figure 6. Forecast scenarios of cyclic gas injection-extraction over 20 years. The initial time of simulation corresponds to 9 June 2013. Red and blue lines represent the injection and extraction phases, respectively. (a) Production data for numerical simulations of scenario 1 with the reference model (Table S3). (b) Production data for scenarios 2 and 3 with the reference and extreme models, respectively. The extreme model differs from the reference model by only three parameters (dip angles of receiver faults = 25°, frictional coefficient = 0.8, reservoir Biot coefficient = 0.8).

4 Results

Following the geomechanical modeling scheme proposed by Jiang et al. (*2020*), we simulate the spatiotemporal evolution of pore pressure and Coulomb failure stress (CFS) perturbation due to cyclic gas injection-extraction of the HUGS using the well-constrained hydro-geomechanical model and the mean rates in a fully-coupled poroelastic framework. Both mechanical and hydraulic boundaries are imposed on the model (Figure S1). The mechanical boundaries include: (I) that the top boundary is a free surface, (II) that the bottom and side boundaries are fixed in the normal directions but free to move in the parallel directions, and (III) that the injection wells are fixed. The hydraulic boundaries comprise no-flow conditions applied for the bottom and side boundaries and zero-pressure condition on the top boundary. Besides, the wells are taken as flux discontinuity boundaries for cyclic gas injection-extraction. To approximate the cylindrical borehole in realistic operation, the specific discharge in our 2D models is calculated by dividing the mean volumetric rates of injection and extraction by the cylindrical surface area of open-hole well sections.

During calculation of CFS changes, the receiver faults are assumed to dip southwestward at an angle of 20°, based on the predominant faulting features in the study area (Figure 5b), which is in accordance with the reported focal mechanisms of the two $M_L \geq 3.0$ events (*Zhou et al., 2019*) and the maximum horizontal compression stress oriented in the NE-SW direction (*Heidbach et al., 2016*) (Figure 1c). As our study focuses on the stress perturbation relative to the start point on 9 June 2013, it is unnecessary to consider the stress changes caused by gas production from 1998 to 2012.

4.1 Physics-based interpretation of seismic distribution and focal mechanisms

The results of our simulations reveal two lobes with elevated CFS on the southwest and northeast sides of the HUGS (Figure 7). The variation of their spatial scales is correlated with the gas injection-extraction cycles (Movie S1). We take the 0.1-bar (10 kPa) stress perturbation as a threshold, which is generally regarded to be the minimum increment in failure stress needed to trigger earthquakes on critically stressed faults (*Stein, 1999*). After 50 days since the onset of gas injection, the northeast lobe with frictional coefficient of the receiver faults equal to 0.4 expanded to a width of 1.24 km (Figure 7b), which coincides with the timing and location of the August

2013 cluster. Moreover, stress variations at the two probing points (P1 and P3) in the regions with positive stress perturbation show that the magnitudes of poroelastic stress changes are much larger than pore pressure (Figure 8). In regions with induced seismicity, the increase of CFS is dominated by the poroelastic stress associated with the reservoir dilatation. Beyond that, Figure 7a also shows that the boundary effects have little influence on the simulation results.

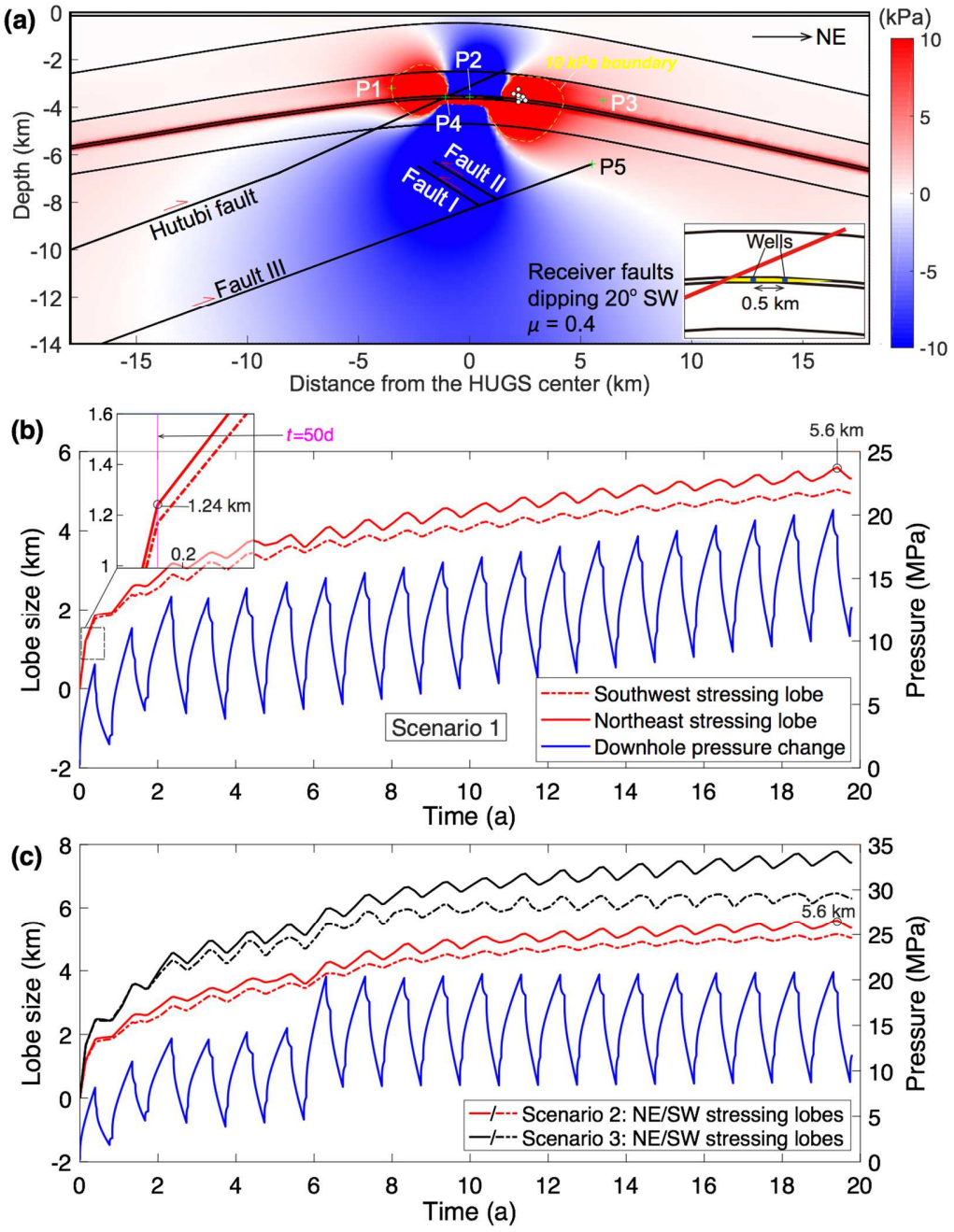

Figure 7. Spatiotemporal evolution of the strength of CFS perturbation. (a) Simulated CFS perturbation at the end of the sixth HUGS injection phase with realistic production data and the reference model (Table S1). Insert panel shows a close-up view of wells. (b-c) Temporal variations of the stressing sidelobe sizes during gas injection-extraction cycles of 20 years. The initial time of simulation corresponds to 9 June 2013. Scenario 1 corresponds to the reference model simulated with the production data in Figure 6a (Table S3). Scenarios 2 and 3 correspond to the reference and extreme models simulated with the production data in Figure 6b. Inset figure in panel (b) shows the close-up view of a time span during the first injection phase. Pink vertical line indicates the initiation time of the August 2013 cluster.

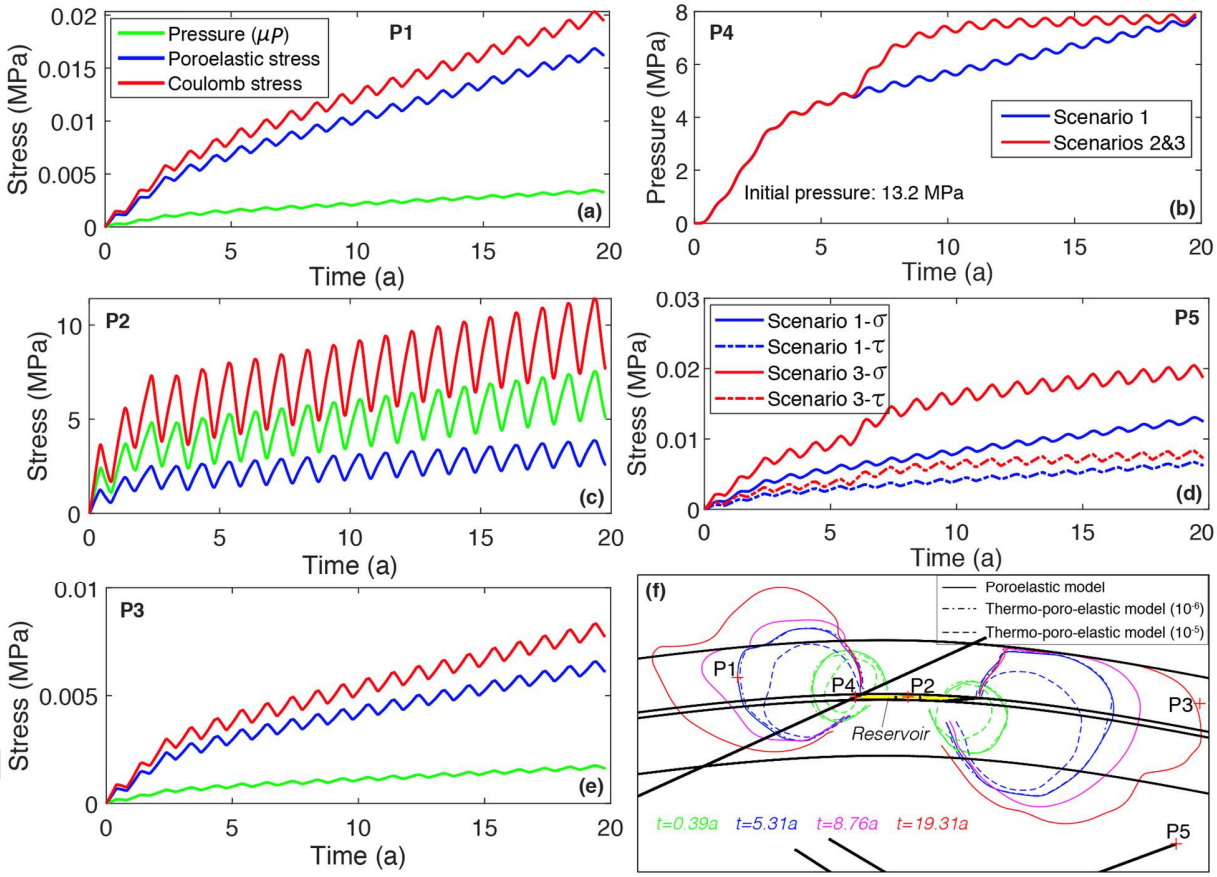

Figure 8. Temporal variations of pressure, poroelastic and CFS perturbation at five probing points. The initial time of simulation corresponds to 9 June 2013. P1-P3 are located in the southwest stressing lobe, the reservoir, and the northeast stressing lobe, respectively. P4 lies within the Hutubi fault zone is used to probe pressure changes. P5 lies within fault III is used to probe normal and shear stresses changes acting on the fault plane. (f) Sizes of the two stressing sidelobes defined by 0.1 bar boundary at four time nodes. Solid and dashed lines show the simulation results without and with consideration of thermoelastic effect, respectively.

In light of these findings, the seismic cluster in August 2013 was likely caused by stress perturbations due to poroelastic loading at the causative fault(s) that exceeded its critical triggering threshold. The spatiotemporal distribution of induced seismicity can be summarized into two explanations. First, the sharp increases in seismicity are associated with seismic clusters that occurred on the secondary faults located in the two stressing lobes rather than the reservoir-bounding Hutubi fault. The occurrence time depends on the distances between the secondary faults and the HUGS, which influence the strength of poroelastic loading. Second, the few sporadic earthquakes surrounding the HUGS are potentially linked to ubiquitous pre-existing faults with scales much smaller than the secondary faults. This kind of faults were most likely brought to rupture by the cyclic nature of gas injection-extraction.

The two $M_L \geq 3.0$ earthquakes are characterized by thrust-slip on faults dipping to the southwest, much like the Hutubi fault. This kind of slip mechanism is also related to the reservoir dilatation, which enhanced shear stresses on the principal focal planes. As the horizontal component of the compression is in line with the NE-SW oriented maximum tectonic principal stress (*Heidbach et al., 2016*) and the predominant faults thrusting northeast-ward (Figure 5b), such faults would be most susceptible to failure in the two stressing lobes, especially during the injection phase of each operational stage.

Our analyses reveal that the spatiotemporal distribution and focal mechanisms of induced earthquakes depend on the poroelastic loading process due to the reservoir dilatation with increasing pore pressure. The variations in stress at probing points P1 and P3 clearly show the loading process is linked to cyclic nature of gas injection-extraction (Figure 8). In addition, contrasts in hydromechanical properties of the geological formations and fault geomechanical parameters can also influence the loading magnitude, which tends to regulate the sharp increase of induced seismicity in partnership with the location of the secondary faults. Accordingly, with no stress transfer by aseismic slip (e.g., *Eyre et al., 2019*) detected in the geodetic observations, the seismicity occurred near the HUGS due to poroelastic loading is a combined effect of both operational and geological factors. Chang et al. (*2020*) also found that both operational and

geological factors control the accumulation process of pressure and poroelastic stress at the Pohang enhanced geothermal system (EGS) site.

4.2 Reactivation potential of the Hutubi fault and fault III

Figure 7a shows that the Hutubi fault and fault III, which are hydraulically connected to and isolated from the reservoir, respectively, pass through the sidelobes characterized by enhanced CFS. Consequently, assessing the largest potential earthquake associated with the HUGS is compounded direct pore pressure effects and poroelastic perturbation. To evaluate the maximum magnitude, we need to first assess the reactivation potentials of these two major known faults. If they are reactivated, the magnitude of the largest potential earthquake would depend on their spatial scales.

The method of slip tendency analysis (equation 6), which is defined as the ratio of shear stress to effective normal stress acting on a fault plane, is used to calculate the potential for frictional failure. Two points within the two fault zones are selected to probe the changes of pore pressure and elastic stress associated with cyclic gas injection-extraction. Point P4 is located at the central depth of the part of the Hutubi fault in the reservoir layer. As the Hutubi fault is hydraulically connected to the wells, we focus on the pore pressure pertubation (Figure 8b). Point P5 is located at the top end of fault III, which is most close to the stressing lobe. As there is no hydraulic connection between fault III and the reservoir, we only consider the changes of normal and shear stresses (Figure 8d).

For the Hutubi fault, we assume that the pore pressure can reach the maximum working pressure of 34 MPa, which is equal to the initial pressure of the reservoir before exploitation of the gas field in 1998 (*Cao, 2013*). This assumption represents an extreme but plausible case where the fault damage zone has a direct hydraulic connection to the injection wells. Then we calculated the shear (τ) and effective normal (σ') stress acting on the Hutubi fault, with dip angles varing from 20° to 25°, as well as the slip tendency (τ/σ') based on the magnitudes of S_{Hmax} and S_V (Table 1). Under two different dip angles, both of the slip tendency estimates are less than 0.15. For fault III, with dip angles varing from 12° to 28°, the normal and shear stress changes at the end of the assumed 20-year gas injection-extraction process are less than 0.03 MPa even under the extreme simulation scenario 3 with the largest stress perturbation (Figure 8d). The slip tendency estimates of fault III

are 0.05-0.09, two to three times lower than the values of the Hutubi fault (Table 1). The sensitivity of these results to parameterization is discussed in Section 5.1.

Table 1. Calculation of slip tendencies of the Hutubi fault and fault III

Hutubi fault	Dip angle	20°	25°
	Shear stress	6.1 MPa	7.3 MPa
	Normal stress	81.5 MPa	82.7 MPa
	Pore pressure	34 MPa	
	Slip tendency	0.13	0.15
Fault III	Dip angle	12°	28°
	Shear stress	3.9 MPa	7.9 MPa
	Normal stress	80.1 MPa	83.5 MPa
	Stress perturbation	0.03 MPa	
	Slip tendency	0.05	0.09

An assumption in the slip tendency calculation is that values below the static frictional coefficient represent stable fault conditions. Indeed, the slip tendencies for both the Hubuti fault and fault III are far smaller than the minimal static frictional coefficient of 0.4 (*Shimamoto & Logan, 1981; Wibberley & Shimamoto, 2005*), indicating an extremely low possibility of fault reactivation without an additional source of loading, whether natural or driven by human activities, or an additional source of fault weakening. In particular, the pore pressure in the Hutubi fault would likely not reach its limit of 34 MPa (Figure 8b). Moreover, the fault stability analyses assume the two faults to be cohesionless, but faults can often be cemented and have an apparent cohesive strength, which may be restored by hydrothermal cementation, quartz solution under temperatures higher than 90°C (*Fisher & Knipe, 1998*), which is close to the reservoir temperature of 92.5°C (*Cao, 2013*). Consequently, our evaluation of the stability of these major faults, with geometries imaged by 3D seismic data, represent conservative results and put a cap on the magnitude of the largest potential earthquake.

4.3 Magnitude of the largest potential earthquake

The evidence at hand indicates that the mechanism leading to induced earthquakes at the HUGS site has thus far been related to poroelastic deformation caused by cyclic gas injection-extraction, which exhibits a strong influence on secondary, southwest-dipping thrust faults. In addition, the slip tendency values of the major faults near the HUGS are much lower than their frictional strength. Therefore, potential earthquakes induced by future operation of the HUGS would most

likely occur on the secondary faults. The magnitude of the largest potential earthquake induced by the HUGS would depend on the scales of such secondary faults. Unfortunately, the secondary fauts cannot be identified from the 3D seismic survey, but the faults illuminated by the earthquake swarms in August 2013, from Tang-2018 and Zhou-2019, are about 1.0 km long (Figure 1c). According to global compilations of stress drop estimates (*Baltay et al., 2010*), we assume that stress drops are independent of magnitude and estimate the maximum magnitude to be around Mw 4.2 based on the scaling relation between moment magnitude and fault length (*Blaser et al., 2010*); this is much smaller than the result (M>7) obtained by Qiao et al. (*2018*) based on the empirical relationship between injection volumes and seismic moment release (*McGarr, 2014*). Our estimate of maximum magnitude is not a statistical result, nor is it dependent of the number of smaller events (e.g., *van der Elst, et al., 2016*).

We caution that it is challenging to assign an unertainty to the maximum magnitude estimate because of myriad sources of epistemic uncertainty, namely the inability to identify secondary faults and the absence of location uncertainties for detected events. Although we cannot be sure that the sizes of secondary faults are limited to ~1 km scales, or that ruptures on separate fault structures would not link together, we are confident that all the major faults in proximity to the HUGS have been identified and that these faults are characterized by very low reactivation potentials. *Mazzoldi et al. (2012)* investigated the maximum earthquake magnitude generated by faults which are too small to be detected by current geophysical surveys. They concluded that CO_2 injection in geological carbon sequestration projects is unlikely to induce a major event (7<M<7.9), but rather of a minor event (2<M<3.9).

4.4 Location of the largest potential earthquake

As the distribution of detected earthquakes is spatially consistent with the stressing sidelobes and their spatiotemporal variation is also correlated with the evolution of the sidelobe sizes (Figure 7), future induced earthquakes would most likely occur in the two sidelobes. To forecast the location of the largest potential earthquake, we consider three different scenarios of future operation (with 14 more years, Table S3) to simulate growth of these sidelobes. Scenario 1 corresponds to simulation with the reference model (Table S1) and future injection and extraction rates equal to the latest (6^{th}) operation cycle. The two other scenarios set the HUGS to reach the design capacity

(10.7 billion m^3) and the maximum design working pressure (34 MPa) at the end of the next (seventh) injection phase; subsequent cycles are then assumed to operate under the maximum pressure and storage capacity. Sensitivity analyses of CFS calculations show that the sidelobe sizes increase with the reservoir Biot coefficients, fault dip angles and frictional coefficients (Section 5.1), we here consider both the reference model and the extreme model (with the largest test values of the three parameters: dip angles of receiver faults = 25°, frictional coefficient = 0.8, reservoir Biot coefficient = 0.8) for the simulations of the two scenarios.

Under scenario 1, the HUGS reservoir reaches the maximum working pressure at the end of the twentieth injection phase (Figure 7b). The growth rate of the sidelobe is greatest during the first several cycles and then grows slowly. Under scenarios 2 and 3, the lobe sizes indeed have a noticeable increase during the seventh injection phase, when the HUGS first reaches the maximum pressure (Figure 7c). However, the sizes increase slightly when the HUGS is under stable operation with equivalent pressure variations, especially during the last several cycles. Interestingly, with two different ways of reaching the maximum pressure (under scenarios 1 and 2), the northeast stressing lobe extends to the same size of 5.6 km at the end of the last injection phase. Even for the extreme case of scenario 3, the northeast lobe size is less than 8 km wide.

The lobe sizes are also affected by the reservoir width, which varies along the strike of the Hutubi fault (Figure 9a). Without a complete set of production data of the first six cycles, we cannot perform realistic 3D geomechanical modeling and accurate analysis of the variation of the lobe sizes. Instead, the influence of different HUGS reservoir widths on the stressing lobe sizes is investigated through 2D modeling with five different widths according to the well locations (Figure 9a). The simulation results of the reference model (Table S1) show that the southwest lobe at the end of the latest injection phase with realistic production data decreases from 4.1 km to 3.5 km (Figures 9b and S4). By comparison, the northeast lobe increases from 3.0 km to 4.0 km. Regions with the largest stress perturbation are located in the northwest and southeast of the HUGS, respectively. Under scenario 3 with the extreme model, the southwest and northeast lobe sizes range from 6.2 km to 5.3 km and from 4.2 km to 5.1 km (Figure S5), respectively. Overall the stressing lobe sizes vary by less than 1 km for the suite of test reservoir widths.

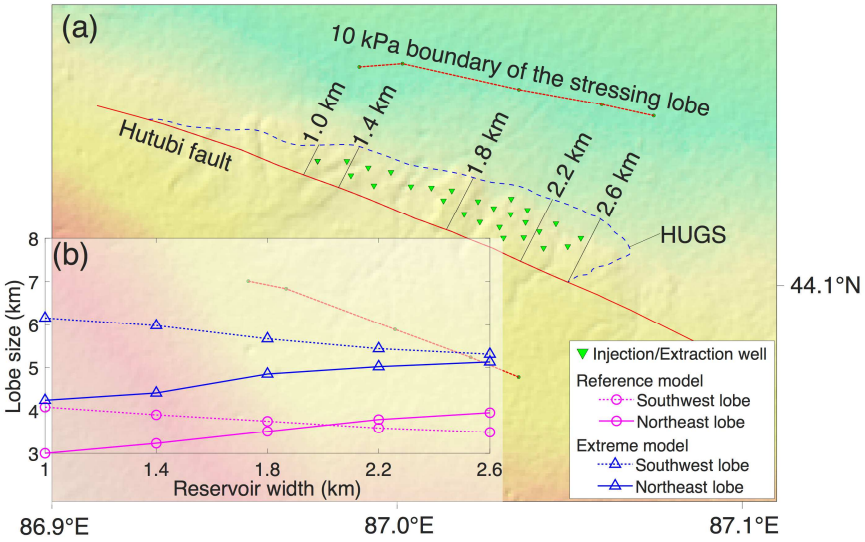

Figure 9. Influence of the HUGS reservoir widths on the sizes of the stressing sidelobes at the end of the sixth injection phase. (a) Locations of five 2D hydro-geomechanical models with different reservoir widths (1.0 to 2.6 km) and 10 kPa boundaries of the two stressing sidelobes (red dashed lines) at the end of the sixth injection phase. (b) Simulated sidelobe sizes with the reference and extreme models. The extreme model is different from the reference model (Table S1) with only three parameters (dip angles of receiver faults = 25°, frictional coefficient = 0.8, reservoir Biot coefficient = 0.8).

Based on our simulation results for future growth of the stressing sidelobes, seismicity induced by the HUGS is likely to be confined within a zone no greater than ~8 km away from the reservoir, under the assumption of a stress triggering threshold equal to 0.1 bar. As the potential induced earthquakes are expected to occur on the secondary faults, with limited scales, the possibility of earthquake rupture extending outside of the perturbed region is very low. Of course, this estimate should be further refined pending access to complete production data and insight into future operational plans.

The strategy to evaluate the magnitude and location of the largest potential earthquake is further verified by 3D simulation tests, which show that the stress changes on the slices cutting through the reservoir are quantitatively close to current 2D simulation results (Figures S6 and S7). Although the faults identified from the 3D seismic survey are assumed to be infinite along the strike direction in the 2D modeling, 3D simulations reveal that the finite scales of faults have a minor effect on the stress calculation at the two (northwest and southeast) ends of the gas reservoir (Figure S7). This would influence the location of the largest potential earthquake at the two ends,

which is why the curves outlining the occurrence range in Figure 9 are not closed. But, in calculating the results of slip tendencies of major faults, we have considered different fault dip angles and the extreme stress perturbation on the faults; these far exceed the effects of finite fault scales.

5 Discussion

With the newly-developed physics-based framework, we have derived the estimates of the maximum magnitude and location of the largest potential earthquake. Interpretation of the spatiotemporal distribution and focal mechanisms of detected earthquakes is taken a key step in this process. There are many studies to interpret the spatiotemporal distribution of induced seimicity (e.g., *Shapiro & Dinske, 2009; Chang & Yoon, 2020; Denlinger & Connell, 2020; Yeo et al., 2020*) or to estimate the seismic risk (e.g., *Mazzoldi et al., 2012; Dempsey & Suckale, 2017; Langenbruch et al., 2018*), but there are not many that do both in an integrated framework. For example, Shapiro and Dinske (*2009*) proposed a general non-linear diffusional (*r*-*t*) equation to derive the triggering front of fluid induced seismicity based on the physical basis of pore pressure perturbation. Chang and Yoon (*2020*) developed a conceptual model to interpret the spatiotemporal patterns of induced seismicity observed at Azle, Texas. They found that fault orientation with respect to local stress perturbations can be one of the critical factors to determine the spatiotemporal pattern of injection-induced seismic events over time.

In addition, our method of interpreting the spatiotemporal distribution of induced seismicity also differs from the seismicity rate model based on the rate/state friction law (*e.g., Dieterich, 1994; Segall & Lu, 2015*) used to interpret the temporal distribution of induced seismicity (*e.g., Candela et al. 2019; Zhai et al., 2019*). Although the rate/state seismicity model uses physical parameters like the background seismicity, stressing rates, and fault frictional properties, it was designed to explain seismicity rates inside a fixed crustal volume, meaning there is an inherent tradeoff between the size of the volume in consideration and the size of faults it may reasonably contain. This makes it difficult to interpret the spatial distribution of seismicity, and says nothing about either the faulting styles of induced earthquakes or the largest potential earthquake. Currently, there has been a growing need for physics-based models that link injection operation to the observed seismicity, and we are able to directly relate the effects of the poroelastic loading processes of cyclic gas injection/extraction to the detected earthquakes. Numerical simulations of

prospective gas storage and extraction activities over the next decade reveal that poroelastic loading effects would also control the largest potential earthquake, which would most likely occur on failure-prone secondary faults with a magnitude around Mw 4.2.

Although preceding simulations have revealed that the spatiotemporal distribution of detected earthquakes matches with the evolution of the stressing sidelobe sizes, the strength of stress perturbation depends on many model parameters, each with its own natural variability. To test the influences of different parameter settings, we here conduct sensitivity analysis on the CFS calculation. In addition, there should be some thermoelastic effects during gas injection phases since the temperature of injected gas is lower than the reservoir termperature, which are not considered in the above modeling, and here we conduct additional simulations to quantitatively investigate the effects.

5.1 Sensitivity tests

As the hydro-geomechanical model has been tightly constrained by multiple geological, geophysical and geodetic data, we here only evaluate the sensitivities of CFS calculations to the assumed dip angles and frictional coefficients of receiver faults, as well as the reservoir Biot coefficients.

First, the geological interpretation of 3D seismic reflection surveying data identifies two kinds of thrust faults dipping to the northeast and southwest, respectively, within the study area (Figure 5). Under the scenario of receiver faults dipping to the southwest, the two stressing lobes rotate counterclockwise and expand from a width of 1.1 km to 1.3 km with dip angles increasing from 10° to 30° at the occurrence time of the August 2013 cluster (Figure 10). Under the scenario of northeast-dipping receiver faults, the stress perturbation is vertically symmetrical with the simulated stress pattern of the preceding scenario.

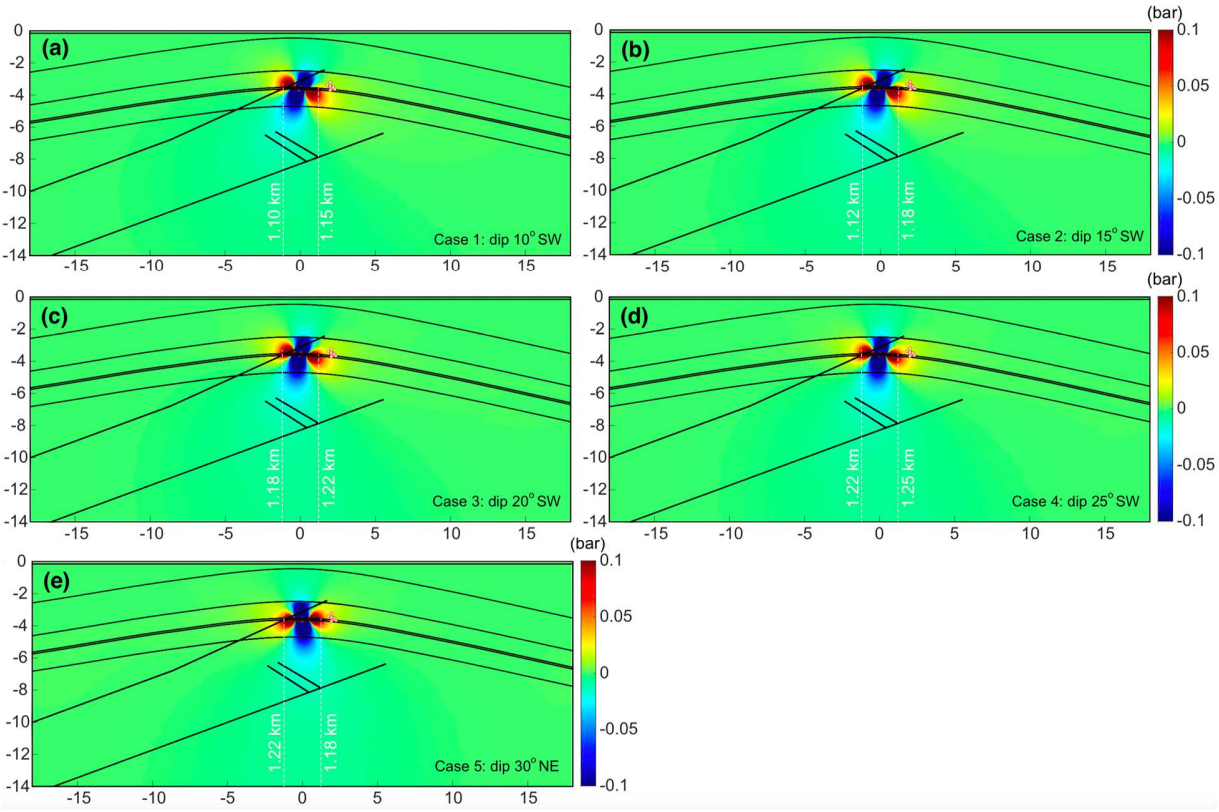

Figure 10. Coulomb failure stress perturbation at the occurrence time of the seismic cluster in August 2013 with five different assumed receiver faults. White dashed lines mark the 0.1-bar boundaries of the two lobes with evaluated CFS. White points show the seismic cluster in August 2013 from Zhou-2019.

Second, for most rocks the static frictional coefficient ranges from 0.6 to 0.85 (*Byerlee, 1978; Townend & Zoback, 2000; Collettini & Sibson, 2001*). In the presence of clay minerals or gouge in the fault zone, the frictional coefficient can be much lower at ~0.4 (*Shimamoto & Logan, 1981; Wibberley & Shimamoto, 2005*). The results from additional simulations show that the aforementioned CFS lobe sizes are relatively insensitive to the assumed friction; they increase from 1.2 km to 1.3 km corresponding to frictional coefficients of 0.4-0.8 (Figure 11).

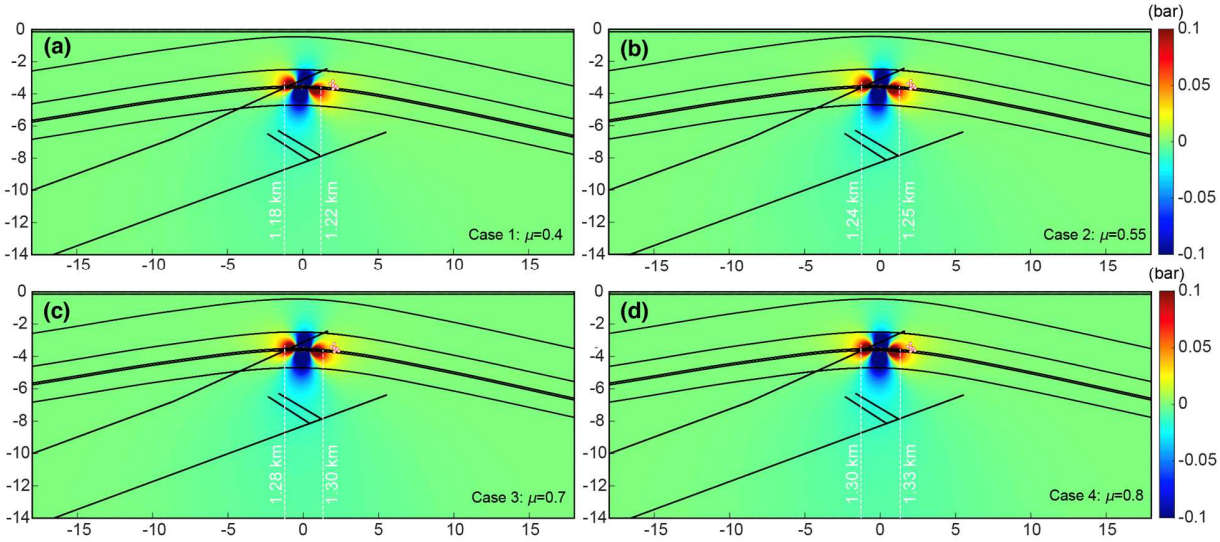

Figure 11. Coulomb failure stress perturbation at the occurrence time of the seismic cluster in August 2013 with different frictional coefficients. White dashed lines mark the 0.1-bar boundaries of the two lobes with evaluated CFS. White points show the seismic cluster in August 2013 from Zhou-2019.

Third, the Biot coefficient α represents the effective stress coefficient for bulk deformation, controlling the strength of coupling between pressure diffusion and elastic deformation, with values ranging from 0 to 1. In the reference geomechanical model (Table S1), α is calculated to be 0.39 based on the drained bulk modulus K and the bulk modulus K_s of the solid constituent according to this relation: $\alpha = 1 - K/K_s$ (*Wang, 2000*). When the value increases from 0.2 to 0.8, the two lobe sizes expand from 0.9 km to 1.6 km (Figure 12). Among the parameter sensitivities we tested, this clearly has the strongest influence on the expansion of the sidelobes. For α=0.8 in particular, the 0.1-bar boundary of the northeast stressing lobe is very close to the distance between the cluster and the HUGS reservoir. Hence, the discrepancy between the lobe size and the distance is probably due to model simplifications including fault angles, frictional and Biot coefficients, hypocentral location uncertainties notwithstanding. Alternatively, the 0.1-bar threshold may be unrealisticly low for faults in this area, but increasing this threshold would shrink the size of the CFS sidelobes.

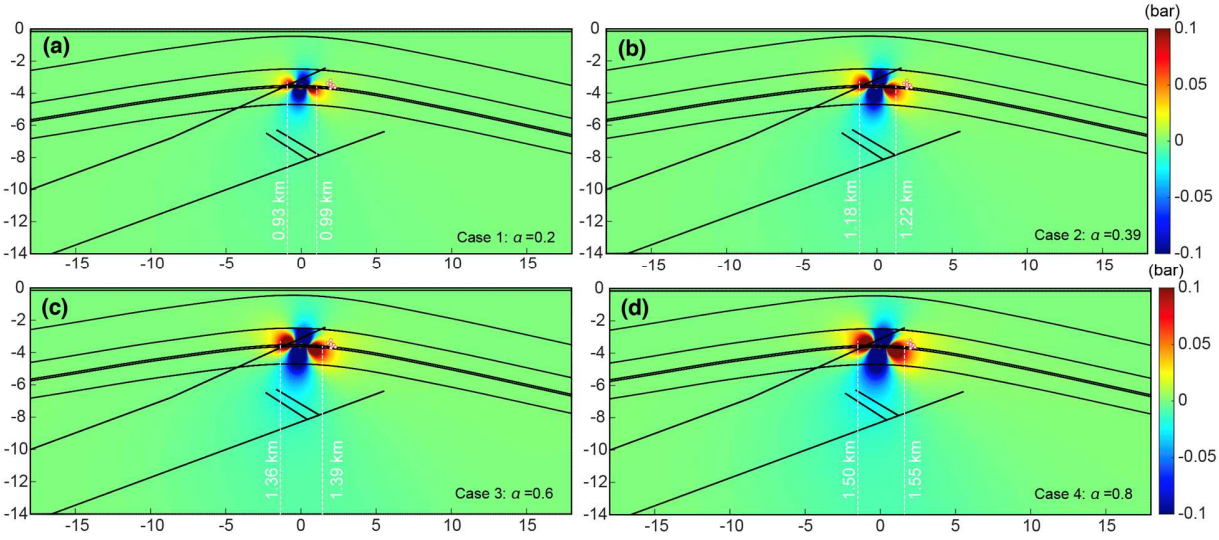

Figure 12. Coulomb failure stress perturbation at the occurrence time of the seismic cluster in August 2013 with different reservoir Biot coefficients. White dashed lines mark the 0.1-bar boundaries of the two lobes with evaluated CFS. White points show the seismic cluster in August 2013 from Zhou-2019.

Lastly, although the reservoir porosity and permeability in our model are selected to be 20% and 3.25×10^{-13} m^2, respectively, the influence of their variations in narrow range (20-30%, 1.25-3.25 $\times$ 10^{-13} m^2) determined by Jiang et al. (*2020*) are expected to have little influence. The major reasons for this include: (1) that the stress changes depend on both porosity and permeability which work together, and (2) that the simulated rock deformation with different pairs of the two paramters within the narrow domain fits the GPS observations of surface deformation equally well. The surface deformation reflects subsurface stress changes.

5.2 Thermoelastic effect

Due to lack of observational constraints on the thermophysical properties of rocks of subsurface formation, preceding geomechanical simulations are conducted based on fully-coupled poroelasticity. Although the influence of fluid property changes due to temperature contrasts between injected gas and the reservoir on the stress evolution is believed to be of second order, the secondary thermoelastic effect needs to be quantitatively clarified.

As introduced in Section 2.3, we include heat transfer in porous media and its coupling with the solid matrix. The thermal conductivity and heat capacity of natural gas are set to be 0.032 W/(m·K) and 2300 J/(kg·K), respectively, based on the databases of National Institute of Standards and Technology (NIST). The thermal conductivities and heat capacities of all rocks are set to be 3 W/(m·K) and 850 J/(kg·K), respectively. Based on the thermal expansion coefficients of rocks (*Skinner, 1966*), we test two values: 10^{-5} and 10^{-6} 1/K. In addition, we set the temperature difference to be 10 K for each injection phase, which is much larger than the median values of injection and extraction temperature.

Our thermo-poroelastic simulations reveal that the Coulomb stress changes in the two sidelobes are slightly less than the magnitudes derived from the reference model (Figure 8f) when thermoelastic effect is considered. At the probing point P1, the simulated CFS with the largest thermal expansion coefficient is only about 19% less than that without considering thermoelastic effect at the end of the sixth injection phase (Figure 13). These results indicate a relatively small difference compared to the changes in pore pressure diffusion within the reservoir; however, without finer observational constraints on the thermophysical properties of the reservoir rock, these should be viewed as relatively coarse estimates. The thermoelastic effect of injecting low-temperature gas indeed causes contraction of rock, but such deformation does not encourage failure on thrust faults, like the ones hosting the two $M_L \geq 3.0$ events in August 2013; hence, we believe the results from simpler poroelastic solutions, which fit GPS-observed ground deformation (*Jiang et al., 2020*), have acceptable accuracy.

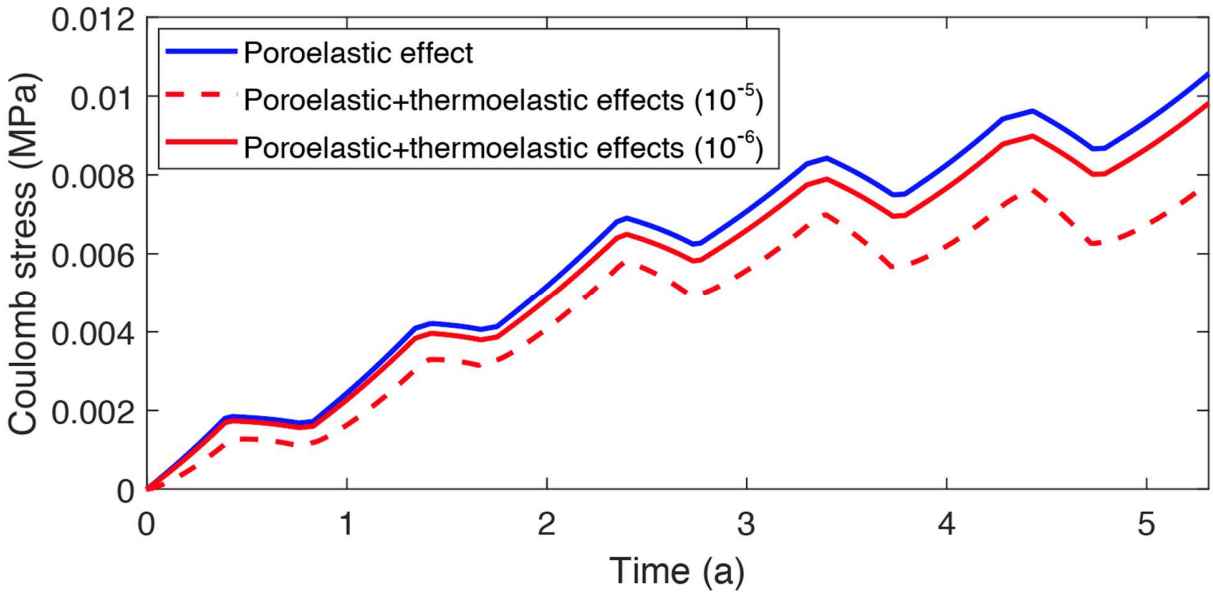

Figure 13. Simulated Coulomb stress changes at the probe point P1 (see Figure 8) with and without consideration of thermoelastic effect.

5.3 Possible reasons for induced seismicity on undiscovered faults

At the HUGS site, the detected earthquakes from the catalog of Zhou-2019 did not occur on the major faults revealed by the 3D seismic survey. This phenomenon – that no clear correlation has been found between faults that are detected by geophysical surveys before injection began and the structures on which seismicity occurred – also exits in other regions with induced seismicity, such as west of Fox Creek, Alberta (*Eaton et al., 2018*), Preston New Road, Lancashire, England (*Clarke et al., 2019*), and St. Gallen deep geothermal project (*Diehl et al., 2019*). The major reason is attributed to the difficulty to detect subtle faults prior to reactivation (*Atkinson et al., 2020; Schultz et al., 2020*). Such fauls are always characterized by very small offsets and are often identified only by the occurrence of earthquakes. Schultz et al. (*2020*) thought that fluid injection (coupled with monitoring of earthquakes) would be one of the best techniques to locate such faults.

Our slip tendency analysis reveals that the reactivation potential of the discovered major faults is extremely low. Although the finding indicates that the crust of our study region is not critically stressed, there are probably some very localized regions with abnormal stress conditions (stress

heterogeneity), which are susceptible to the perturbation of cyclic gas injection-extraction. This could be a possible reason for induced seismicity occurring in a non-critically stressed region.

6 Conclusions

The annual cycle of gas injection-extraction of the HUGS causes measurable ground deformation and induced seismicity. The latter tends to occur during the injection phase of each operation stage. We estimate the magnitude and location of the largest potential earthquake with a physics-based framework founded on fully-coupled poroelastic simulations and a robust hydro-geomechanical model of the system, which can integrate realistic Coulomb failure stress calculations with slip tendency analysis. It is clear that both induced seismic distribution and moment release are controlled by poroelastic loading effect due to the reservoir dilatation; the contrast in temperatures between the reservoir and injected fluid is relatively inconsequential.

The reservoir-bounding Hutubi fault does indeed experience pore pressure increases during cyclic gas injection-extraction, but its orientation in the local stress field dictates that pore pressure changes would need to be substantially larger than the maximum working pressure of the HUGS reservoir to cause frictional failure. Instead, like with the induced earthquakes already observed, the most likely location for future seismicity is on the secondary faults in the sidelobes with enhanced failure stresses where poroelastic loading dominates. Our simulations of more than a decade of hypothetical operational cyles indicate a relatively slow growth of these sidelobes. In this case, and more generally, direct pore pressure and strain monitoring could help confirm this.

Our study helps to provide a reference strategy to assess the source(s) of induced seismicity hazard at UGS facilities, and perhaps more generally. The appraisal process includes physical interpretation of the spatiotemporal distribution and focal mechanisms of induced earthquakes, which can improve the reliability of the evaluation. Additionally, this appraisal process is based largely on commonly collected geophysical datasets like continuous geodetic and seismic data. Thus, with close interdisciplinary cooperation among industry, academia and regulatory authorities, an acceptable balance between energy development activities and exposure of publics to the associated risks may be achieved.

Acknowledgments

We are grateful to Teng-fong Wong, who suggested investigating the influence of the reservoir Biot coefficient and provided financial support for this study. This paper also benefits from insightful comments by Dominik Zbinden (ETH Zurich), U.S. Geological Survey internal reviews from Justin Rubinstein, Nick Beeler and Elizabeth S. Cochran, and discussion with Yajing Liu (McGill University). We would also like to thank David Dempsey and an anonymous reviewer for their critiques during the paper submission process. We appreciate PetroChina for providing 3D seismic reflection data. Any use of trade, firm, or product names is for descriptive purposes only and does not imply endorsement by the U.S. government.

Funding: This study was supported by the NSFC/RGC Joint Research Scheme (N_CUHK418/15 and N_CUHK430/16), Hong Kong Scholars Program, CUHK Research Fellowship Scheme (4200555), National Key R&D Program of China (2018YFC1504104), and RGC-Germany Joint Research Scheme (G-CUHK408/19).

Competing interests: The authors are not aware of any competing interests.

Data and materials availability: Earthquake catalogs are available from Tang et al. (2018) (https://doi.org/10.1029/2018JB015863), Zhou et al. (2019) (https://doi.org/10.1029/2019JB017360), and China Earthquake Data Center (http://data.earthquake.cn). 3D seismic reflection data supporting this research are not accessible to the public or research community due to the confidentiality agreement with PetroChina, which may be available by contacting corresponding authors. The production data is obtained from Jiang et al. (2020) (https://doi.org/10.1016/j.epsl.2019.115943) and some online reports (detailed weblinks are presented in Table S2).

References

Afshari Moein, M. J., T. Tormann, B. Valley, & S. Wiemer (2018). Maximum magnitude forecast in hydraulic stimulation based on clustering and size distribution of early microseismicity. *Geophys. Res. Lett.* 45, 6907-6917. doi:10.1029/2018GL077609.

Atkinson, G. M., Eaton, D. W., & Igonin, N. (2020). Developments in understanding seismicity triggered by hydraulic fracturing. *Nature Reviews Earth & Environment*, 1–14. doi:10.1038/s43017-020-0049-7

Baltay, A., G. Prieto, & G. C. Beroza (2010), Radiated seismic energy from coda measurements and no scalingin apparent stress with seismic moment, *J. Geophys. Res.* 115, B08314, doi:10.1029/2009JB006736.

Blaser, L., F. Kruger, M. Ohrnberger, F. Scherbarun (2010). Scaling Relations of Earthquake Source Parameter Estimates with Special Focus on Subduction Environment. *Bull. Seismol. Soc. Am.* 100 (6), 2914–2926.

Biot, M. A. (1941). General theory of three-dimensional consolidation, *J. Appl. Phys*., 12, 155–164.

Byerlee, J. D. (1978). Friction of rocks. *Pure Appl. Geophys.* 116, 615–626.

Candela, T., Osinga, S., Ampuero, J.□P., Wassing, B., Pluymaekers, M., Fokker, P. A., et al. (2019). Depletion□induced seismicity at the Groningen gas field: Coulomb rate□and□state models including differential compaction effect. *J. Geophys. Res.* 124, 7081–7104. doi:10.1029/2018JB016670

Cao, X. (2013). A research on reservoir geomechanics features of a gas storage in Xinjiang after natural depletion. Ph.D. thesis, China University of Geoscience, Beijing.

Chang, K. W., & P. Segall (2016), Injection-induced seismicity on basement faults including poroelastic stressing, *J. Geophys. Res.* 121, 2708–2726, doi:10.1002/2015JB012561.

Chang, K. W., & Yoon, H. (2020). Hydromechanical controls on the spatiotemporal patterns of injection-induced seismicity in different fault architecture: Implication for 2013–2014 Azle earthquakes. *J. Geophys. Res*. 125, e2020JB020402. doi:10.1029/2020JB020402

Chang, K. W., Yoon, H., Kim, Y. H., & Lee, M. Y. (2020). Operational and geological controls of coupled poroelastic stressing and pore-pressure accumulation along faults: Induced earthquakes in Pohang, South Korea. *Sci. Rep.* 10, 2073. doi:10. 1038/s41598-020-58881-z

Chen, X., Nakata, N., Pennington, C., et al. (2017). The Pawnee earthquake as a result of the interplay among injection, faults and foreshocks. *Sci. Rep.* 7, 4945, doi:10.1038/s41598-017-04992-z.

Clarke, H., Verdon, J. P., Kettlety, T., Baird, A. F. & Kendall, J.-M. (2019). Real- time imaging, forecasting, and management of human- induced seismicity at Preston New Road, Lancashire, England. *Seismol. Res. Lett.* 90, 1902–1915.

Cochran, E.S., Skoumal, R.J., McPhillips, D., Ross, & Z.E., Keranen (2020), Activation of optimally and unfavourably oriented faults in a uniform local stress field during the 2011 Prague, Oklahoma, sequence, *Geophys. J. Int. 2*22 (1), 153–168, doi:10.1093/gji/ggaa153

Collettini, C., & R. H. Sibson (2001). Normal faults, normal friction? *Geology* 29, 927–930.

Dempsey, D., Kelkar, S., Pawar, R., Keating, E., & Coblentz, D. (2014). Modeling caprock bending stresses and their potential for induced seismicity during CO2 injection. *Int. J. Greenhouse Gas Control* 22, 223–236. doi:10.1016/j.ijggc.2014.01.005

Dempsey, D., & J. Suckale (2017). Physics-based forecasting of induced seismicity at Groningen gas field, the Netherlands, *Geophys. Res. Lett.* 44, 7773–7782, doi:10.1002/2017GL073878.

Denlinger, R. P., & D. R. H. O'Connell (2020). Evolution of Faulting Induced by Deep Fluid Injection, Paradox Valley, Colorado, *Bull. Seismol. Soc. Am.* 110, 2308–2327, doi: 10.1785/0120190328

Diehl, T., Kraft, T., Kissling, E. & Wiemer, S. (2017).The induced earthquake sequence related to the St. Gallen deep geothermal project (Switzerland): Fault reactivation and fluid interactions imaged by microseismicity. *J. Geophys. Res.* 122, 7272–7290.

Dieterich, J. (1994), A constitutive law for rate of earthquake production and its application to earthquake clustering, *J. Geophys. Res.* 99(B2), 2601–2618.

Dieterich, J. H., K. B. Richards-Dinger, & K. A. Kroll (2015). Modeling injection-induced seismicity with the physics-based earthquake simulator RSQSim, *Seismol. Res. Lett.* 86(4), 1102–1109, doi: 10.1785/0220150057.

Eaton, D. W., Igonin, N., Poulin, A., Weir, R., Zhang, H., Pellegrino, S., & Rodriguez, G. (2018). Induced seismicity characterization during hydraulic□fracture monitoring with a shallow□wellbore geophone array and broadband sensors. *Seismol. Res. Lett.* 89(5), 1641–1651. doi:10.1785/0220180055

Ellsworth, W. L. (2013). Injection-induced earthquakes. *Science* 341 (6142).

Eyre, T. S., D. W. Eaton, D. I. Garagash, M. Zecevic, M. Venieri, R. Weir, & D. C. Lawton (2019). The role of aseismic slip in hydraulic fracturing–induced seismicity. *Sci. Adv.* 5, eaav7172.

Fisher, Q. J., & R. J. Knipe (1998). Fault sealing processes in siliciclastic sediments. In: Jones, G., Fisher, Q.J. & Knipe, R.J. (eds) Faulting, Fault Sealing and Fluid Flow in Hydrocarbon Reservoirs. Geological Society, London, Special Publications, 147, 117–134.

Gaite, B., A. Ugalde, A. Villasenor, & E. Blanch (2016), Improving the location of induced earthquakes associated with an underground gas storage in the Gulf of Valencia (Spain), *Phys. Earth Planet. Inter.* 254, 46–59.

Galis, M., J. P. Ampuero, P. M. Mai, & F. Cappa (2017). Induced seismicity provides insight into why earthquake ruptures stop. *Sci. Adv.* 3, eaap7528.

Heidbach, O., M. Rajabi, K. Reiter, & M. Ziegler (2016). World Stress Map 2016. GFZ Data Services, doi: 10.5880/WSM.2016.002

Hope, A. C. (1968). A simplified Monte Carlo significance test procedure. *J. Royal Stat. Soc.* 30(3), 582-598, doi:10.1111/j.2517-6161.1968.tb00759.x

Jiang, G., X. Qiao, X. Wang, R. Lu, L. Liu, H. Yang, Y. Su, L. Song, B. Wang, & T.-f. Wong (2020). GPS observed horizontal ground extension at the Hutubi (China) underground gas storage facility and its application to geomechanical modeling for induced seismicity. *Earth Planet. Sci. Lett.* doi:10.1016/j.epsl.2019.115943.

Keranen, K. M., M. Weingarten, G. A. Abers, B. A. Bekins, & S. Ge (2014). Sharp increase in central Oklahoma seismicity since 2008 induced by massive wastewater injection. *Science* 345 (6195), 448-451.

Kim, K.□H., Ree, J.□H., Kim, Y., Kim, S., Kang, S.□Y., & Seo, W. (2018). Assessing whether the 2017 MW Pohang earthquake in South Korea was an induced event. *Science*. doi:10.1126/science.aat6081

King, G. C. P., & R. S. Stein, J. Lin (1994). Static stress changes and the triggering of earthquakes, *Bull. Seismol. Soc. Am.* 84, 935–953.

Kwiatek, G., P. Martínez-Garzón, G. Dresen, M. Bohnhoff, H. Sone, & C. Hartline (2015). Effects of long-term fluid injection on induced seismicity parameters and maximum magnitude in northwestern part of The Geysers geothermal field, *J. Geophys. Res.* 120, 7085–7101, doi:10.1002/2015JB012362.

Langenbruch, C., & M. D. Zoback (2016). How will induced seismicity in Oklahoma respond to decreased saltwater injection rates? *Sci. Adv.* 2, e1601542.

Langenbruch, C., M. Weingarten, & M. D. Zoback (2018). Physics-based forecasting of man-made earthquake hazards in Oklahoma and Kansas. *Nature Communications* 9, 3946, doi:10.1038/s41467-018-06167-4.

Lee, K.-K., W. L. Ellsworth, D. Giardini, J. Townend, S. Ge, T. Shimamoto, I.-W. Yeo, T.-S. Kang, J. Rhie, D.-H. Sheen, C. Chang, J.-U. Woo, & C. Langenbruch (2019). Managing injection-induced seismic risks, *Science* 364 (6442).

Lei, X., Z. Wang, & J. Su (2019). The December 2018 M_L 5.7 and January 2019 M_L 5.3 earthquakes in South Sichuan basin induced by shale gas hydraulic fracturing. *Seismol. Res. Lett.* 90(3), 1099-1110.

Lu, R., Y. Liu, X. Xu, X. Tan, D. He, G. Yu, M. Cai, & X. Wu (2019). Three- dimensional model of the lithospheric structure under the eastern Tibetan Plateau: Implications for the active tectonics and seismic hazards. *Tectonics*, doi:10.1029/2018TC005239

Maerten, L., Gillespie, P., & Daniel, J.-M. (2006). Three-dimensional geomechanical modeling for constraint of subseismic fault simulation. *AAPG Bulletin* 90(9), 1337–1358. doi:10.1306/03130605148

Maurer, J., & P. Segall (2018). Magnitudes of Induced Earthquakes in Low-Stress Environments, *Bull. Seismol. Soc. Am.* 108, 1087–1106, doi:10.1785/0120170295.

Mazzoldi, A., Rinaldi, A. P., Borgia, A., & Rutqvist, J. (2012). Induced seismicity within geological carbon sequestration projects: Maximum earthquake magnitude and leakage potential from undetected faults. *Int. J. Greenhouse Gas Control* 10, 434–442. doi:10.1016/j.ijggc.2012.07.012

McGarr, A. (2014). Maximum magnitude earthquakes induced by fluid injection, *J. Geophys. Res.* 119, 1008–1019, doi:10.1002/2013JB010597.

McGarr, A., B. Bekins, N. Burkardt, J. Dewey, P. Earle, W. Ellsworth, S. Ge, S. Hickman, A. Holland, E. Majer, J. Rubinstein, & A. Sheehan (2015). Coping with earthquakes induced by fluid injection. *Science* 347 (6224), 830-831.

McGarr, A. & N. C. Gay (1978). State of stress in the Earth's crust. *Annual Review of Earth and Planetary Sciences* 6, 405.

Morris, A., Ferril, D. A., & Henderson, D. B. (1996). Slip tendency analysis and fault reactivation. *Geology* 24(3),275–8.

Nield D. A., & Bejan A. (2006). Convection in porous media. New York, NY, USA: Springer.

Norbeck, J. H., & R. N. Horne (2018). Maximum magnitude of injection-induced earthquakes: A criterion to assess the influence of pressure migration along faults. *Tectonophysics* 733, 108-118.

Norbeck, J. H., & Rubinstein, J. L. (2018). Hydromechanical earthquake nucleation model forecasts onset, peak, and falling rates of induced seismicity in Oklahoma and Kansas. *Geophys. Res. Lett.* 45, 2963–2975, doi:10.1002/2017GL076562

Pang, J., G. Qian, B. Wang, Z. Yang, Y. Wei, & Y. Li (2012). Evaluation of sealing ability of underground gas storage converted from the Xinjiang H gas field. *Natural Gas Industry* 32(2), 1-3.

Petersen, M. D., Mueller, C. S., Moschetti, M. P., Hoover, S. M., Rukstales, K. S., McNamara, D. E., Williams, R. A., Shumway, A. M., Powers, P. M., Earle, P. S., Llenos, A. L., Michael, A. J., Rubinstein, J. L., Norbeck, J. H., & Cochran, E. S. (2018). 2018 one- year seismic hazard forecast for the Central and Eastern United States from induced and natural earthquakes, *Seismol. Res. Lett.* 89(3), 1049-1061. doi:10.1785/0220180005.

Priolo, E., et al. (2015), Seismic monitoring of an underground natural gas storage facility: The Collalto Seismic Network, *Seismol. Res. Lett.*, 86(1), 109–123, doi:10.1785/0220140087.

Qiao, X., W. Chen, D. Wang, Z. Nie, Z. Chen, J. Li, X. Wang, Y. Li, T. Wang, & G. Feng (2018). Crustal deformation in the Hutubi underground gas storage site in China observed by GPS and InSAR measurements. *Seismol. Res. Lett.* 89(4), 1467-1477.

Rice, J. R., & M. P. Cleary (1976). Some basic stress diffusion solutions for fluid-saturated porous media with compressible constituents, *Rev. Geophys.* 14, 227–241.

Richter, G., Hainzl, S., Dahm, T. et al. (2020), Stress-based, statistical modeling of the induced seismicity at the Groningen gas field, The Netherlands, *Environ. Earth Sci.* 79, 252, doi:10.1007/s12665-020-08941-4

Rutqvist, J., Rinaldi, A. P., Cappa, F., Jeanne, P., Mazzoldi, A., Urpi, L., et al (2016). Fault activation and induced seismicity in geological carbon storage – Lessons learned from recent modeling studies. *Journal of Rock Mechanics and Geotechnical Engineering*, 8(6), 789–804. doi:10.1016/j.jrmge.2016.09.001

Schultz, R., G. Atkinson, D. W. Eaton, Y. J. Gu, & H. Kao (2018). Hydraulic fracturing volume is associated with induced earthquake productivity in the Duvernay play. *Science* 359 (6373), 304-308.

Schultz, R., Skoumal, R. J., Brudzinski, M. R., Eaton, D., Baptie, B., & Ellsworth, W. (2020). Hydraulic Fracturing Induced Seismicity. *Reviews of Geophysics*. doi:10.1029/2019rg000695

Segall, P. (2000). Earthquake and Volcano Deformation, Princeton Univ. Press, Princeton, N. J.

Segall, P., & S. Lu (2015), Injection-induced seismicity: Poroelastic and earthquake nucleation effects, *J. Geophys. Res. Solid Earth*, 120, 5082–5103, doi:10.1002/2015JB012060.

Shapiro, S. A., & Dinske, C. (2009). Fluid-induced seismicity: Pressure diffusion and hydraulic fracturing. *Geophysical Prospecting*, 57(2), 301–310. doi:10.1111/j.1365-2478.2008.00770.x

Shapiro, S. A., O. S. Krüger, C. Dinske, & C. Langenbruch (2011). Magnitudes of induced earthquakes and geometric scales of fluid-stimulated rock volumes, *Geophysics*, 76(6), WC55–WC63, doi:10.1190/GEO2010-0349.1.

Shaw, J. H., C. Connors, & J. Suppe (2005). Seismic Interpretation of Contractional Fault-related Folds: An AAPG Seismic Atlas. Tulsa: American Association of Petroleum Geologists, 1–156.

Shimamoto, T., & J. M. Logan (1981). Effects of simulated clay gouges on the sliding behavior of Tennessee sandstone. *Tectonophysics* 75, 243–55.

Skinner, B. J. (1966). Thermal expansion. In: S.J. Clark (Editor), Handbook of Physical Constants. *Geol. Sot. Am., Mem.*, 97.

Stein, R. S. (1999). The role of stress transfer in earthquake occurrence. *Nature* 402, 605-609.

Streit, J. E., & R. R. Hillis (2004). Estimating fault stability and sustainable fluid pressures for underground storage of CO2 in porous rock. *Energy* 29, 1445–1456.

Suppe, J., 1983. Geometry and kinematics of fault-bend folding. *American Journal of Science*, 283, 684–721.

Tang, L., Z. Lu, M. Zhang, L. Sun, & L. Wen (2018). Seismicity induced by simultaneous abrupt changes of injection rate and well pressure in Hutubi gas field. *J. Geophys. Res.* 123(7), 5929–5944.

Townend, J., & M. D. Zoback (2000). How faulting keeps the crust strong. *Geology* 28, 399–402.

van der Elst, N. J., M. T. Page, D. A. Weiser, T. H. W. Goebel, & S. M. Hosseini (2016). Induced earthquake magnitudes are as large as (statistically) expected, *J. Geophys. Res.* 121, 4575–4590, doi:10.1002/2016JB012818.

Wang, H. (2000). Theory of Linear Poroelasticity With Applications to Geomechanics and Hydrogeology, Princeton Univ. Press, Princeton, N. J.

Wang, S., Jiang, G., Weingarten, M., & Niu, Y. (2020). InSAR evidence indicates a link between fluid injection for salt mining and the Changning (China) earthquake sequence. *Geophys. Res. Lett.*, doi:10.1029/2020GL087603.

Weingarten, M., S. Ge, J. W. Godt, B. A. Bekins, & J. L. Rubinstein (2015). High-rate injection is associated with the increase in U.S. mid-continent seismicity. *Science* 348 (6241), 1336-1340.

Wibberley, C. A. J., & T. Shimamoto (2005). Earthquake slip weakening and asperities explained by thermal pressurization. *Nature* 436, 689–692, doi:10.1038/nature03901.

Wu, J., J. Suppe, R. Lu, & R. Kanda (2016). Philippine Sea and East Asian plate tectonics since 52 Ma constrained by new subducted slab reconstruction methods. *J. Geophys. Res.* 121, doi:10.1002/2016JB012923.

Yeck, W. L., Block, L. V., Wood, C. K., & King, V. M. (2015). Maximum magnitude estimations of induced earthquakes at Paradox Valley, Colorado, from cumulative injection volume and geometry of seismicity clusters. *Geophysical Journal International*, 200(1), 322–336. doi:10.1002/2013JB0101597.

Yeo, I. W., Brown, M. R. M., Ge, S., & Lee, K. K. (2020). Causal mechanism of injection-induced earthquakes through the Mw 5.5 Pohang earthquake case study. *Nat. Comm.* 11(1). doi:10.1038/s41467-020-16408-0

Zbinden, D., Rinaldi, A. P., Diehl, T., & Wiemer, S. (2020). Hydromechanical Modeling of Fault Reactivation in the St. Gallen Deep Geothermal Project (Switzerland): Poroelasticity or Hydraulic Connection? *Geophys. Res. Lett.*, doi:10.1029/2019GL085201.

Zhai, G., M. Shirzaei, M. Manga, & X. Chen (2019). Pore pressure diffusion, enhanced by poroelastic stresses, controls induced seismicity in Oklahoma, *Proceeding of National Academy of Science* 116(33), 16228-16233.

Zhou, P., H. Yang, B. Wang, & J. Zhuang (2019). Seismological investigations of induced earthquakes near the Hutubi underground gas storage facility. *J. Geophys. Res.*, doi:10.1029/2019JB017360.

Zöller, G., & M. Holschneider (2016). The Maximum Possible and the Maximum Expected Earthquake Magnitude for Production-Induced Earthquakes at the Gas Field in Groningen, The Netherlands. *Bull. Seismol. Soc. Am.* 106, 2917–2921, doi:10.1785/0120160220.